Atomistic simulations of magnetoelastic effects on sound velocity

P. Nieves [1,*] J. Tranchida,[2] S. Nikolov,[3] A. Fraile [4] and D. Legut [1]

[1]*IT4Innovations, VŠB - Technical University of Ostrava, 17. listopadu 2172/15, 70800 Ostrava-Poruba, Czech Republic*

[2]*CEA, DES/IRESNE/DEC, 13018 Saint Paul Lès Durance, France*

[3]*Computational Multiscale Department, Sandia National Laboratories, P.O. Box 5800, MS 1322, 87185 Albuquerque, New Mexico, USA*

[4]*Nuclear Futures Institute, Bangor University, Bangor, LL57 1UT, United Kingdom of Great Britain and Northern Ireland*

(Received 1 February 2022; revised 14 March 2022; accepted 7 April 2022; published 26 April 2022)

In this work, we leverage atomistic spin-lattice simulations to examine how magnetic interactions impact the propagation of sound waves through a ferromagnetic material. To achieve this, we characterize the sound wave velocity in BCC iron, a prototypical ferromagnetic material, using three different approaches that are based on the oscillations of kinetic energy, finite-displacement derived forces, and corrections to the elastic constants, respectively. Successfully applying these methods within the spin-lattice framework, we find good agreement with the Simon effect including high-order terms. In analogy to experiments, morphic coefficients associated with the transverse and longitudinal waves propagating along the [001] direction are extracted from fits to the fractional change in sound velocity data. The present efforts represent an advancement in magnetoelastic modeling capabilities which can expedite the design of future magnetoacoustic devices.

DOI: 10.1103/PhysRevB.105.134430

I. INTRODUCTION

Magnetoelastic (MEL) interactions are responsible for many interesting phenomena in magnetic materials [1] such as Joule magnetostriction [2], the Wiedemann effect [3], the Villari effect [1], the Matteucci effect [4], anomalous thermal expansion [5], and many others [1,6,7]. MEL coupling also leads to complex effects on sound velocity that took about four decades, from the first works by Fuchs [8] in 1936 and Mueller [9] in 1940 until the comprehensive study by Rouchy *et al.* [10] in 1979, to fully understand [1,11]. Four main magnetic effects on sound velocity have been identified: (i) isotropic exchange effects [8,12], (ii) anisotropic morphic effects [10,13,14], (iii) field dependent effects (the Simon effect) [15–17] and (iv) rotational-magnetostrictive effects [10,11]. J. Rouchy and E. du Tremolet de Lacheisserie provided a detailed theoretical derivation of these four effects for cubic crystals by expanding the internal energy as a series of the Lagrangian tensor components, as well as symmetrical and antisymmetrical components of the homogeneous strains [10]. S. Rinaldi and G. Turilli showed that MEL effects on sound velocity can be equivalently taken into account as corrections to the elastic constants [18]. These MEL effects can be large, and have been experimentally observed in many materials through the dependency of ultrasonic sound wave velocity on the intensity and direction of an applied magnetic field [1,11,17,19–24]. Novel magnetoacoustic phenomena have been discovered in recent years, like acoustic spin pumping [25] and magnetization switching induced by sound waves [26–31], with potential technological applications in spintronics and magnetic recording [32].

Classical atomistic simulations lie between quantum mechanical calculations at microscopic scale and continuum mechanics at macroscopic scale, and bridge the gap between these two scales within a multi-scale modeling approach [33–36]. Atomistic methods are useful in the study of quasiparticle phenomenology like phonon-magnon interactions [37], temperature effects [38], dynamics and nonequilibrium phenomena [34], crystal phase transformation [39], grain boundaries [40], crystal defects [41], and nanostructures [42]. While continuum mechanics methods have been used to model magnetoacoustic phenomena successfully [30,43], atomistic simulations of magnetic effects on sound waves were quite challenging until recently. This phenomenon involves a coupled dynamics of magnetic moments and atoms, so that it is not possible to use only standard atomistic spin dynamics (SD) or molecular dynamics (MD) since the motion of atoms or spins are neglected, respectively [44–46]. An alternative approach could be to combine spin-polarized ab-inito molecular dynamics and SD [47]. This strategy is very accurate but unfortunately is quite demanding computationally, so that it might not a be a convenient method due to the large atomic supercells required to study sound waves. To overcome this limitation, one could couple spin dynamics with molecular dynamics (SD-MD) [37,48–52], also referred as spin-lattice dynamics, thus enabling the simulation of both large system sizes and time scales [50,52]. Recent advances in atomistic models based on spin-lattice simulations offer the possibility of studying MEL phenomena computationally [52,53]. In our previous work, we presented a methodology based on the Néel model to build a classical spin-lattice Hamiltonian for cubic crystals capable of describing magnetic properties induced by the spin-orbit coupling (SOC) like magnetocrystalline anisotropy (MCA) and anisotropic magnetostriction, as well as exchange magnetostriction [54].

*Corresponding author: pablo.nieves.cordones@vsb.cz

Here, we probe the range of applicability of these models by simulating the MEL effects on sound velocity. Such kind of atomistic simulations may be useful to clarify and further understand the physics of this complex phenomenon, as well as speed-up the design of possible novel technological applications based on these effects.

II. METHODOLOGY

A. Spin-lattice Hamiltonian

For the atomistic spin-lattice simulations, we consider the following Hamiltonian:

$$\mathcal{H}_{\rm sl}(\boldsymbol{r},\boldsymbol{p},\boldsymbol{s}) = \mathcal{H}_{\rm mag}(\boldsymbol{r},\boldsymbol{s}) + \sum_{i=1}^{N}\frac{\boldsymbol{p}_i}{2m_i} + \sum_{i,j=1}^{N}\mathcal{V}(r_{ij}), \tag{1}$$

where $\boldsymbol{r}_i$, $\boldsymbol{p}_i$, $\boldsymbol{s}_i$, and m_i stand for the position, momentum, normalized magnetic moment and mass for each atom i in the system, respectively, $\mathcal{V}(r_{ij}) = \mathcal{V}(|\boldsymbol{r}_i - \boldsymbol{r}_j|)$ is the interatomic potential energy and N is the total number of atoms in the system with total volume V. Here, we include the following interactions in the magnetic energy:

$$\mathcal{H}_{\rm mag}(\boldsymbol{r},\boldsymbol{s}) = -\mu_0\sum_{i=1}^{N}\mu_i\boldsymbol{H}\cdot\boldsymbol{s}_i - \frac{1}{2}\sum_{i,j=1,i\neq j}^{N}J(r_{ij})\boldsymbol{s}_i\cdot\boldsymbol{s}_j + \mathcal{H}_{\rm Néel}(\boldsymbol{r},\boldsymbol{s}), \tag{2}$$

where μ_i is the atomic magnetic moment, μ_0 is the vacuum permeability, $\boldsymbol{H}$ is the external magnetic field, $J(r_{ij})$ is the exchange parameter. The term $\mathcal{H}_{\rm Néel}$ is the Néel interaction

$$\mathcal{H}_{\rm Néel} = -\frac{1}{2}\sum_{i,j=1}^{N}\Bigg\{g(r_{ij}) + l_1(r_{ij})\Big[(\boldsymbol{e}_{ij}\cdot\boldsymbol{s}_i)(\boldsymbol{e}_{ij}\cdot\boldsymbol{s}_j) - \frac{\boldsymbol{s}_i\cdot\boldsymbol{s}_j}{3}\Big] + q_1(r_{ij})\Big[(\boldsymbol{e}_{ij}\cdot\boldsymbol{s}_i)^2 - \frac{\boldsymbol{s}_i\cdot\boldsymbol{s}_j}{3}\Big]\Big[(\boldsymbol{e}_{ij}\cdot\boldsymbol{s}_j)^2 - \frac{\boldsymbol{s}_i\cdot\boldsymbol{s}_j}{3}\Big] + q_2(r_{ij})[(\boldsymbol{e}_{ij}\cdot\boldsymbol{s}_i)(\boldsymbol{e}_{ij}\cdot\boldsymbol{s}_j)^3 + (\boldsymbol{e}_{ij}\cdot\boldsymbol{s}_j)(\boldsymbol{e}_{ij}\cdot\boldsymbol{s}_i)^3]\Bigg\}, \tag{3}$$

where $\boldsymbol{e}_{ij} = \boldsymbol{r}_{ij}/r_{ij}$, and

$$l_1(r_{ij}) = l(r_{ij}) + \frac{12}{35}q(r_{ij}),$$
$$q_1(r_{ij}) = \frac{9}{5}q(r_{ij}),$$
$$q_2(r_{ij}) = -\frac{2}{5}q(r_{ij}). \tag{4}$$

In the case of a collinear state ($\boldsymbol{s}_i \parallel \boldsymbol{s}_j$), the Eq. (3) is reduced to

$$\mathcal{H}_{\rm Néel} = -\frac{1}{2}\sum_{i,j=1}^{N}\Bigg[g(r_{ij}) + l(r_{ij})\Big(\cos^2\psi_{ij} - \frac{1}{3}\Big) + q(r_{ij})\Big(\cos^4\psi_{ij} - \frac{6}{7}\cos^2\psi_{ij} + \frac{3}{35}\Big)\Bigg], \tag{5}$$

where $\cos\psi_{ij} = \boldsymbol{e}_{ij}\cdot\boldsymbol{s}_i$. The Néel energy reproduces the correct symmetry of MCA and MEL energy [55]. The quantity $g(r_{ij})$ is set to

$$g(r_{ij}) = J(r_{ij}), \tag{6}$$

in order to offset the exchange interaction, as detailed in Ma *et al.* [48]. This offset of the exchange energy does not affect the precession dynamics of the spins. However, it allows to offset the corresponding mechanical forces. Without this additional term, the forces and the pressure generated by the magnetic Hamiltonian are not zero at its energy ground state (corresponding to the ferromagnetic state). By doing so, the function $g(r_{ij})$ can also be related to the volume magnetostriction ω_s induced by the exchange interactions [54,56]. On the other hand, the dipole ($l(r_{ij})$) and quadrupole ($q(r_{ij})$) terms can describe the effects induced by SOC like the anisotropic magnetostriction and MCA, respectively [54,56]. In this work, the spatial dependence of $J(r_{ij})$, $l(r_{ij})$ and $q(r_{ij})$ is described using the Bethe-Slater curve, as implemented in the SPIN package of LAMMPS [52]

$$J(r_{ij}) = 4\alpha_J\Big(\frac{r_{ij}}{\delta_J}\Big)^2\Big[1 - \gamma_J\Big(\frac{r_{ij}}{\delta_J}\Big)^2 e^{-(\frac{r_{ij}}{\delta_J})^2}\Big]\Theta(R_{c,J} - r_{ij}),$$
$$l(r_{ij}) = 4\alpha_l\Big(\frac{r_{ij}}{\delta_l}\Big)^2\Big[1 - \gamma_l\Big(\frac{r_{ij}}{\delta_l}\Big)^2 e^{-(\frac{r_{ij}}{\delta_l})^2}\Big]\Theta(R_{c,l} - r_{ij}),$$
$$q(r_{ij}) = 4\alpha_q\Big(\frac{r_{ij}}{\delta_q}\Big)^2\Big[1 - \gamma_q\Big(\frac{r_{ij}}{\delta_q}\Big)^2 e^{-(\frac{r_{ij}}{\delta_q})^2}\Big]\Theta(R_{c,q} - r_{ij}), \tag{7}$$

where $\Theta(R_{c,n} - r_{ij})$ is the Heaviside step function and $R_{c,n}$ ($n = J, l, q$) are the cutoff radii. The parameters α_n, γ_n, and δ_n ($n = J, l, q$) must be determined in order to reproduce the Curie temperature (T_C), magnetostriction and MCA, as described in Sec. II B.

The dynamics of spins and atoms are achieved by integrating the following equations of motion [57]:

$$\frac{d\boldsymbol{r}_i}{dt} = \{\boldsymbol{r}_i, \mathcal{H}_{\rm sl}\},$$
$$\frac{d\boldsymbol{p}_i}{dt} = \{\boldsymbol{p}_i, \mathcal{H}_{\rm sl}\},$$
$$\frac{d\boldsymbol{s}_i}{dt} = \{\boldsymbol{s}_i, \mathcal{H}_{\rm sl}\}, \tag{8}$$

where

$$\{F, G\} = \sum_{i=1}^{N}\Big(\frac{dF}{d\boldsymbol{r}_i}\cdot\frac{dG}{d\boldsymbol{p}_i} - \frac{dG}{d\boldsymbol{r}_i}\cdot\frac{dF}{d\boldsymbol{p}_i} - \frac{\boldsymbol{s}_i}{\hbar}\Big[\frac{dF}{d\boldsymbol{s}_i}\times\frac{dG}{d\boldsymbol{s}_i}\Big]\Big). \tag{9}$$

In this work, we focus on MEL effects at zero-temperature, so that Langevin thermostats are not included in Eqs. (8) [52]. In Appendix C, we provide some tests to verify the correct implementation of the applied magnetic field and anisotropy field in spin-lattice simulations.

B. Spin-lattice model for BCC Fe

We study the MEL effects on sound velocity for BCC Fe at zero-temperature. To build the spin-lattice model for this material, we follow the procedure described in Ref. [54]. For the classical interatomic potential $\mathcal{V}(r_{ij})$, we use the spectral neighbor analysis potential (SNAP) [58] for BCC

TABLE I. Parameters of the SD-MD model for BCC Fe.

SD-MD model parameters	BCC Fe
α_l (μeV/atom)	377.32
γ_l	0.78979
δ_l (Å)	2.45105
$R_{c,l}$ (Å)	2.6
α_q (μeV/atom)	29.965
γ_q	1.0496
δ_q (Å)	2.45105
$R_{c,q}$ (Å)	2.6
α_J (meV/atom)	−14.2048
γ_J	2.6125
δ_J (Å)	2.45105
$R_{c,J}$ (Å)	2.6

Fe developed by Nikolov *et al.* [53], that yields very good agreement with first-principles calculations. The magnetoelastic contribution to this potential is modified in order to improve its predictions of magnetostrictive properties. The calculated parameters of the Bethe-Slater curve for $J(r_{ij})$ and the Néel dipole and quadrupole terms are given in Table I. We use an effective short-range parametrization of the Bethe-Slater curve [54] for $J(r_{ij})$ in order to reproduce experimental Curie temperature $T_C = 1043$ K [59] and theoretical volume magnetostriction $\omega_s = (V_0^c - V_0^r)/V_0^r$ (where V_0^c and V_0^r are the equilibrium volumes at the collinear state and paramagnetic-like state, respectively) calculated by Shimizu using the itinerant electron model [60], that is $\omega_s = 1.16 \times 10^{-2}$. The equilibrium lattice parameter is obtained from the analysis of the equation of state (EOS) as in Ref. [54]. Namely, we compute the energy for a set of unit cells with different lattice parameter (volume), and fit these data to the Murnaghan EOS [61,62] which gives the equilibrium volume as a fitting parameter. From this analysis we find that the equilibrium lattice parameter for the collinear state without SOC of BCC Fe is $a_0^c = 2.83023$ Å, and for the state with randomly oriented magnetic moments (paramagnetic-like state) is $a_0^r = 2.81937$ Å. Randomly oriented (no short-range order) magnetic moments that are independent of one another, can be applied to examine paramagnetic states past the Curie temperature, as is done in the disordered local moment framework for example. This is particularly true for iron, where the short-range order of the spins quickly deteriorates past the Curie temperature. The random distribution of the spins is made with the implemented random generator of the SPIN package [52] of LAMMPS [46] with seed number 31.

The elastic constants (C_{ij}), anisotropic magnetostrictive coefficients and MCA given by this model are shown in Table II, which are calculated combining the AELAS [63] and MAELAS [64] packages, both interfaced with LAMMPS [54]. The elastic constants for the state with randomly oriented magnetic moments are calculated using a supercell size of $30 \times 30 \times 30$ unit cells (54 000 atoms). For the magnetic moment we use the experimental values at zero pressure and zero temperature $\mu_{Fe} = 2.2\mu_B$ [59], while for the mass we use 55.85 g/mole.

C. Computational calculation of sound velocity

To calculate the sound velocity, we use three different approaches based on (i) the oscillation of the kinetic energy [69], (ii) the finite displacement method [70] (FDM), and (iii) corrections to elastic constants [18]. Below we provide some details about these methods.

1. Oscillation of the kinetic energy

The first method makes use of the oscillation of the kinetic energy to derive the sound velocity [69]. Namely, as the initial condition for spin-lattice dynamics, one displaces the atoms to generate a standing plane wave with sufficiently large wavelength (isolated phonon with low momentum $\boldsymbol{k}_{\rm ph}$)

$$\boldsymbol{u}(\boldsymbol{r}, t) = \boldsymbol{u}_0 \cos(\boldsymbol{k}_{\rm ph} \cdot \boldsymbol{r}) \cos(2\pi f_{\rm ph} t), \tag{10}$$

where $\boldsymbol{u}$ is the displacement vector, $\boldsymbol{u}_0$ is the displacement amplitude, $f_{\rm ph}$ is the frequency of the phonon, $\boldsymbol{r}$ is the position and t is the time. Here, periodic boundary conditions are used, and $k_{\rm ph} = 2\pi n/L$, where n is an integer and L is the length of the simulated system along $\boldsymbol{k}_{\rm ph}$. Next, one runs spin-lattice dynamics (with initial velocities of atoms equal to zero to simulate sound velocity at zero temperature) using the microcanonical ensemble NVE for at least few periods of the kinetic energy. In our simulation, we set the time step $dt = 1$ fs, and we verify that the total energy is preserved. Last, the phonon

TABLE II. Calculated and experimental elastic constants, MEL constants (b_i), magnetostrictive coefficients (λ), MCA (K_1), saturation magnetization (M_s), and density (ρ) for BCC Fe at zero temperature. The elastic constants are calculated assuming collinear (C_{ij}^c) and randomly (C_{ij}^r) oriented atomic magnetic moments without SOC, as explained in the main text.

Elastic constants	C_{ij}^c SD-MD (GPa)	C_{ij}^r SD-MD (GPa)	Expt. (GPa)	b	SD-MD (MPa)	Expt. (MPa)	λ	SD-MD ($\times 10^{-6}$)	Expt. ($\times 10^{-6}$)	K_1 SD-MD (kJ/m^3)	K_1 Expt. (kJ/m^3)	$\mu_0 M_s$ SD-MD (T)	$\mu_0 M_s$ Expt. (T)	ρ^c SD-MD (g/cm^3)	ρ^r SD-MD (g/cm^3)
C_{11}	252.56	256.60	243[a]	b_1	−4.41	−3.3[e]	λ_{001}	26.08	26[c]	55.001	55[d]	2.26	2.19[c]	8.18	8.28
C_{12}	139.87	143.84	138[a]	b_2	9.73	10.5[e]	λ_{111}	−30.33	−30[c]						
C_{44}	106.95	119.99	122[a]												

[a]Reference [65].
[b]Reference [66].
[c]Reference [59].
[d]Reference [67].
[e]Reference [68].

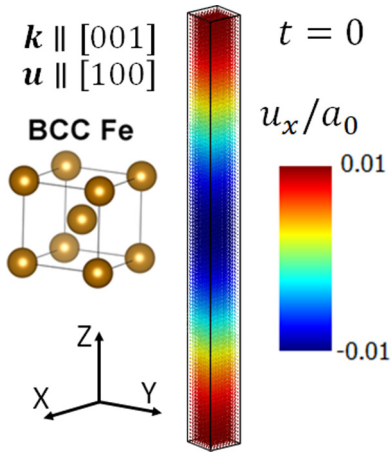

FIG. 1. Initial atomic displacement of a transverse phonon mode propagating in the direction $\boldsymbol{k}_{\rm ph} \parallel [001]$ with polarization $\boldsymbol{u} \parallel [100]$ for BCC Fe. The system size is $10 \times 10 \times 120$ unit cells, while the displacement amplitude is $u_0 = 0.01a_0$. The phonon momentum is $k_{\rm ph} = 2\pi/(120a_0)$.

frequency $f_{\rm ph}$ is extracted from the fitting of the kinetic energy (E_K) versus time [69]

$$E_K(t) = A[1 - \cos(4\pi f_{\rm ph} t)], \tag{11}$$

where A is a fitting parameter that does not depend on time since no attenuation of the sound wave takes place due to the lack of energy dissipation for these particular simulation conditions. Here, in the limit of low momentum ($k_{\rm ph} \to 0$), the phonon's velocity (group velocity) $v_{\rm ph}$ approaches the sound velocity v in the solid (continuum theory) that can be expressed in terms of the elastic constants. For example, in the case of a sound wave propagating in the direction [001], one can approximately compute the sound velocity in the solid from the phonon's frequency and momentum as

$$v\Big|_{\boldsymbol{u}}^{\boldsymbol{k}\parallel[001]} = \lim_{k_{\rm ph}\to 0} v_{\rm ph}\Big|_{\boldsymbol{u}}^{\boldsymbol{k}_{\rm ph}\parallel[001]} = \frac{2\pi f_{\rm ph}}{k_{\rm ph}}\Big|_{\boldsymbol{u}}^{\boldsymbol{k}_{\rm ph}\parallel[001]}. \tag{12}$$

In our calculations, we use a system size $10 \times 10 \times 120$ unit cells (24 000 atoms, $L = 120a_0$) with lattice parameter a_0^c and low phonon momentum $n = 1$ ($k_{\rm ph} = 2\pi/(120a_0)$) for BCC Fe at collinear state, see Fig. 1. In the case of paramagnetic-like state, we increase the system size up to $30 \times 30 \times 120$ unit cells (216 000 atoms) with lattice parameter a_0^r, as discussed in Sec. IV A. The simulations are performed using the SPIN package [52] of LAMMPS [46]. As first benchmark of this method, we study the influence of the displacement amplitude $\boldsymbol{u}_0$ on the calculated frequency for a transverse phonon propagating in the direction $\boldsymbol{k}_{\rm ph} \parallel [001]$ with polarization $\boldsymbol{u} \parallel [100]$. The results are shown in Fig. 2. We see that below $u_0 = 0.01a_0$ the frequency is not significantly affected by this parameter, so we use this value for our calculations. The fitting to extract the frequency for this case (collinear state without SOC) is shown in Fig. 3. The calculated velocity using Eq. (12) with the fitted frequency $f_{\rm ph}^c$ and the value of $k_{\rm ph}^c = 2\pi/(120a_0^c)$ is $v_{\rm ph}^c = 3602.2$ m/s. Note that in this method to further reduce the phonon's momentum ($k_{\rm ph} \to 0$), one needs to increase the system size (L) making the simulations more demanding computationally. On the other hand, one advantage of this method is that could be used to study the MEL effects on the attenuation of sound waves [1,15,17,69] through the time dependence of the fitting parameter $A(t)$ in Eq. (11) within a simulation that allows energy dissipation. The study of MEL effects on the attenuation of sound waves is not performed in the present work.

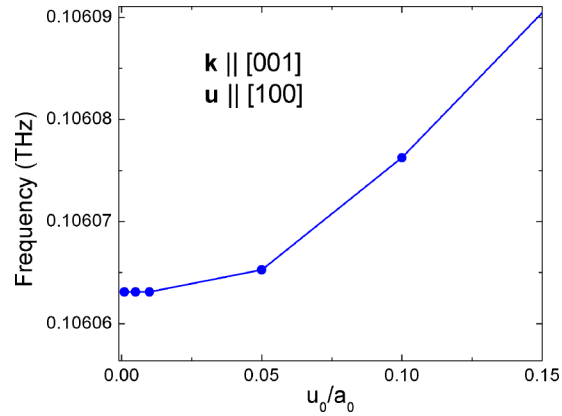

FIG. 2. Calculated frequency vs the initial displacement amplitude u_0 of a phonon propagating in the direction $\boldsymbol{k}_{\rm ph} \parallel [001]$ with polarization $\boldsymbol{u} \parallel [100]$ for BCC Fe at the collinear state without SOC.

2. *Finite displacement method*

To overcome the size limitations of the method based on the oscillation of the kinetic energy, one can use the FDM [70]. In the FDM, the phonon's frequency is derived from the forces associated with a systematic set of displacements. Here, we use this method, as implemented in the program PHONOPY [70,71], also leveraging the PHONOLAMMPS [72] interface between PHONOPY and LAMMPS. The group velocity of the phonon is computed as [71]

$$v_{\rm ph}(\boldsymbol{k}, j) = \frac{1}{4\pi f_{\rm ph}(\boldsymbol{k}, j)} \langle \boldsymbol{e}(\boldsymbol{k}, j)| \frac{\partial D(\boldsymbol{k})}{\partial \boldsymbol{k}} |\boldsymbol{e}(\boldsymbol{k}, j)\rangle, \tag{13}$$

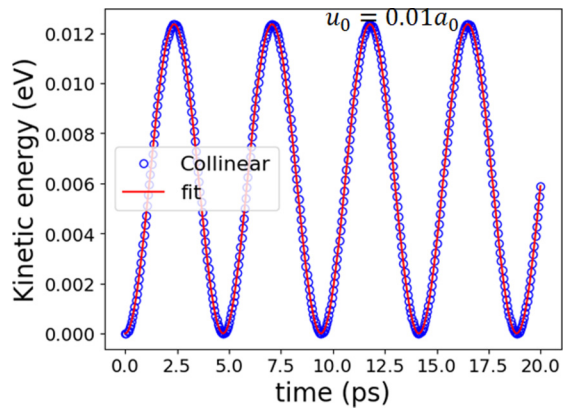

FIG. 3. Fitting to extract the frequency from the oscillation of the kinetic energy of a transverse standing wave propagating in the direction $\boldsymbol{k} \parallel [001]$ with polarization $\boldsymbol{u} \parallel [100]$ for BCC Fe at the collinear state without SOC. Blue points stand for the calculation with spin-lattice simulations, while the red line represents the fitting to Eq. (11).

where j is the phonon's band index, D is the dynamical matrix, and $\boldsymbol{e}$ is the phonon polarization vector. For the collinear calculations we generate a supercell with size $4 \times 4 \times 4$ with lattice parameter a_0^c, while for the paramagnetic states, we use $16 \times 16 \times 16$ with lattice parameter a_0^r. We find that good convergence in group velocity is observed for these cell sizes. The atomic displacement distance is set to its default value 0.01 Å. Since in this method we do not have size limitations for studying phonons with very low momentum ($k_{\rm ph} \to 0$), we compute the frequency and group velocity for a phonon with momentum $k_{\rm ph} = 2\pi/(12\,000 a_0)$. For example, in the case of a transverse phonon at a collinear state propagating in the direction $\boldsymbol{k}_{\rm ph} \parallel [001]$ with very low momentum $\boldsymbol{k} = (0, 0, 2\pi/(12\,000 a_0^c))$, the calculated group velocity with the FDM is $v_{\rm ph}^c = 3601.2$ m/s, which is quite close to the value obtained with the oscillation of the kinetic energy ($v_{\rm ph}^c = 3602.2$ m/s).

3. Corrections to elastic constants

As third method, we consider the MEL effects as corrections to elastic constants. A detailed description of this approach is given in Appendix A. For example, in the case of a transverse sound wave propagating in the direction $\boldsymbol{k}_{\rm ph} \parallel [001]$ with polarization $\boldsymbol{u} \parallel [100]$ at a collinear state without SOC, we have

$$v^c\Big|_{\boldsymbol{u}\parallel[100]}^{\boldsymbol{k}\parallel[001]} = \sqrt{\frac{C_{44}^c}{\rho^c}}, \tag{14}$$

where ρ^c is the density of the material at the collinear state. Using the elastic constant C_{44}^c and density ρ^c (see Table II) at the collinear state in Eq. (14), we find $v^c = 3615.7$ m/s. Although slightly larger than the previously simulated phonon's velocity with the oscillation of the kinetic energy and FDM, this remains within a close agreement.

III. THEORY OF MAGNETOELASTIC EFFECTS ON SOUND VELOCITY

In this section, we provide a brief overview of the main theoretical isotropic and anisotropic MEL effects on sound velocity. To facilitate the analysis of the simulations, it is convenient to decompose the isotropic and anisotropic MEL effects on the fractional change in velocity as follows:

$$\begin{aligned}
&\frac{v^{\rm SOC} - v^r}{v^r} \\
&= \frac{v^c - v^r}{v^r} + \frac{v^{\rm SOC} - v^c}{v^r} \\
&= \frac{v^c - v^r}{v^r} + \frac{v^{\rm SOC} - v^c}{v^c} \frac{1}{1 - \left(\frac{v^c - v^r}{v^c}\right)} \\
&= \frac{v^c - v^r}{v^r} + \frac{v^{\rm SOC} - v^c}{v^c}\left[1 + \left(\frac{v^c - v^r}{v^c}\right) + \dots\right] \\
&\simeq \frac{v^c - v^r}{v^r} + \frac{v^{\rm SOC} - v^c}{v^c} + O\left[\left(\frac{v^{\rm SOC} - v^r}{v^c}\right)\left(\frac{v^c - v^r}{v^c}\right)\right],
\end{aligned} \tag{15}$$

where $v^{\rm SOC}$ is the sound velocity at a collinear state including isotropic exchange and SOC interactions, v^r is the sound velocity assuming randomly oriented atomic magnetic moments (paramagnetic-like state) including only isotropic exchange interaction, and v^c is the sound velocity at a collinear state including only isotropic exchange interaction. In the last step, we assumed that the change in the sound velocity due to MEL effects is small in comparison to the sound velocity ($|v^{\rm SOC} - v^c|/v^c \ll 1$, $|v^c - v^r|/v^r \ll 1$), which is a reasonable approximation for the spin-lattice model used here (see Sec. IV).

In experiment, the sound velocity is typically measured through the pulse echo method [73]. The measured frequency with this technique F is related to the sound velocity v and sample length l along the direction of the wave propagation through the following equation [20,73,74]:

$$v(F, l) = 2Fl. \tag{16}$$

Performing a Taylor expansion of sound velocity yields

$$\begin{aligned}
v(F, l) &= v(F_0, l_0) + \left(\frac{\partial v}{\partial F}\right)_{l=l_0}(F - F_0) \\
&\quad + \left(\frac{\partial v}{\partial l}\right)_{F=F_0}(l - l_0) \\
&= v_0 + 2l_0(F - F_0) + 2F_0(l - l_0),
\end{aligned} \tag{17}$$

where $v(F_0, l_0) = v_0 = 2F_0 l_0$. If we subtract v_0 from both sides of Eq. (17) and divide both sides by v_0, then we obtain [1,10]

$$\frac{v - v_0}{v_0} = \frac{F - F_0}{F_0} + \frac{l - l_0}{l_0}. \tag{18}$$

The theoretical expressions for the fractional change in pulse echo frequency F have been derived by Rouchy *et al.* [1,10,11]. In addition to this contribution, in Eq. (18), we see that the fractional change in length along the direction of wave propagation must be also calculated in order to compute the fractional change in velocity. This fractional change in length arises from the magnetostriction induced by MEL interactions, and its general form for an arbitrary measuring length direction $\boldsymbol{\beta}$ is given by Eq. (B8).

The first term in the right-hand side of Eq. (15) corresponds to the fractional change in sound velocity due to the isotropic exchange interaction (isotropic MEL effects) [1,10]

$$\begin{aligned}
\frac{v^c - v^r}{v^r}\Big|_{\boldsymbol{u}}^{\boldsymbol{k}} &= \frac{F^c - F^r}{F^r}\Big|_{\boldsymbol{u}}^{\boldsymbol{k}} + \frac{l^c - l^r}{l^r}\Big|^{\boldsymbol{k}}, \\
\frac{F^c - F^r}{F^r}\Big|_{\boldsymbol{u}}^{\boldsymbol{k}} &= Y\left(m_i^{\alpha,2}\right)\Big|_{\boldsymbol{u}}^{\boldsymbol{k}},
\end{aligned} \tag{19}$$

where $Y(m_i^{\alpha,2})$ is a function that depends on the isotropic morphic coefficients $m_i^{\alpha,2}$. The form of this function also depends on the propagation direction of the wave $\boldsymbol{k}$ and polarization $\boldsymbol{u}$ but not on the magnetization direction $\boldsymbol{M}$, since this MEL effect is isotropic. In this isotropic case, the fractional change in length depends only on the propagation direction of the wave. The second term in the right hand side of Eq. (15) gives the anisotropic MEL effects due to the SOC, and may

be splitted into the following terms [1,10,11]:

$$\left.\frac{v^{\mathrm{SOC}}-v^{c}}{v^{c}}\right|_{\boldsymbol{u}}^{\boldsymbol{k},\boldsymbol{M}}=\left.\frac{F^{\mathrm{SOC}}-F^{c}}{F^{c}}\right|_{\boldsymbol{u}}^{\boldsymbol{k},\boldsymbol{M}}+\left.\frac{l^{\mathrm{SOC}}-l^{c}}{l^{c}}\right|^{\boldsymbol{k},\boldsymbol{M}},$$
$$\left.\frac{F^{\mathrm{SOC}}-F^{c}}{F^{c}}\right|_{\boldsymbol{u}}^{\boldsymbol{k},\boldsymbol{M}}=G\left(m_{i}^{\gamma,2},m_{i}^{\varepsilon,2}\right)\Big|_{\boldsymbol{u}}^{\boldsymbol{k},\boldsymbol{M}}+R\left(\lambda^{\gamma,2},\lambda^{\varepsilon,2}\right)\Big|_{\boldsymbol{u}}^{\boldsymbol{k},\boldsymbol{M}}+S(H)\Big|_{\boldsymbol{u}}^{\boldsymbol{k},\boldsymbol{M}},\tag{20}$$

where $G(m_i^{\gamma,2}, m_i^{\varepsilon,2})$ is a function that depends on anisotropic morphic coefficients $m_i^{\gamma,2}$ and $m_i^{\varepsilon,2}$ which are linear combinations of second order in strain MEL constants and third order in strain elastic constants, $R(\lambda^{\gamma,2}, \lambda^{\varepsilon,2})$ is a function that comes from rotational and magnetostrictive effects [11] and depends on anisotropic magnetostrictive coefficients $\lambda^{\gamma,2}$ and $\lambda^{\varepsilon,2}$, and $S(H)$ is a field-dependent term derived by Simon [15]. The form of these functions also depends on $\boldsymbol{k}$, $\boldsymbol{u}$ and $\boldsymbol{M}$. The fractional change in length depends on $\boldsymbol{k}$ and $\boldsymbol{M}$ but not on the polarization $\boldsymbol{u}$. The relationship between the morphic coefficients and higher order elastic and MEL constants are given in Eq. (B10), where we use the same definitions as in Ref. [11]. Equations (19) and (20) are derived from the free energy by solving the coupled elastic and magnetic equations of motion [1,10,11,15,75]. A theoretical description of all these effects can also be provided by expanding the internal energy as a series of the Lagrangian tensor components, as well as symmetrical and antisymmetrical components of the homogeneous strains [10]. The explicit form of these equations for the simulated cases is shown in Sec. IV. Alternatively, one can also take into account MEL effects on sound velocity as corrections to the elastic constants [1,18]. We describe this approach in Appendix A.

IV. RESULTS

A. Isotropic magnetoelastic effects

In the case of a transverse wave propagating along $\boldsymbol{k} \parallel [001]$ with polarization $\boldsymbol{u} \parallel [100]$, Eq. (19) reads [10]

$$\left.\frac{v^{c}-v^{r}}{v^{r}}\right|_{\boldsymbol{u}\parallel[100]}^{\boldsymbol{k}\parallel[001]}=\left.\frac{F^{c}-F^{r}}{F^{r}}\right|_{\boldsymbol{u}\parallel[100]}^{\boldsymbol{k}\parallel[001]}+\left.\frac{l^{c}-l^{r}}{l^{r}}\right|^{\boldsymbol{k}\parallel[001]},$$
$$\left.\frac{F^{c}-F^{r}}{F^{r}}\right|_{\boldsymbol{u}\parallel[100]}^{\boldsymbol{k}\parallel[001]}=Y\left(m_{i}^{\alpha,2}\right)\Big|_{\boldsymbol{u}\parallel[100]}^{\boldsymbol{k}\parallel[001]}=\frac{m_{3}^{\alpha,2}}{12C_{44}^{c}},$$
$$\left.\frac{l^{c}-l^{r}}{l^{r}}\right|^{\boldsymbol{k}\parallel[001]}=\frac{a_{0}^{c}-a_{0}^{r}}{a_{0}^{r}},\tag{21}$$

where $m_3^{\alpha,2}$ is an isotropic morphic coefficient defined in Eq. (B10). The form of function Y is the same as in Ref. [10], but note that it is not the same as in Ref. [1] due to a different definition of morphic coefficients and high-order MEL constants. The fractional change in length along [001] arises from volume magnetostriction ω_s due to the exchange interaction. Here, to calculate v^r we consider two types of paramagnetic-like state: (i) with randomly oriented magnetic moments along 3D directions (noncollinear spins), and (ii) random up-down (antiparallel spins) orientations [76]. To simulate the purely isotropic MEL effects, we do not include

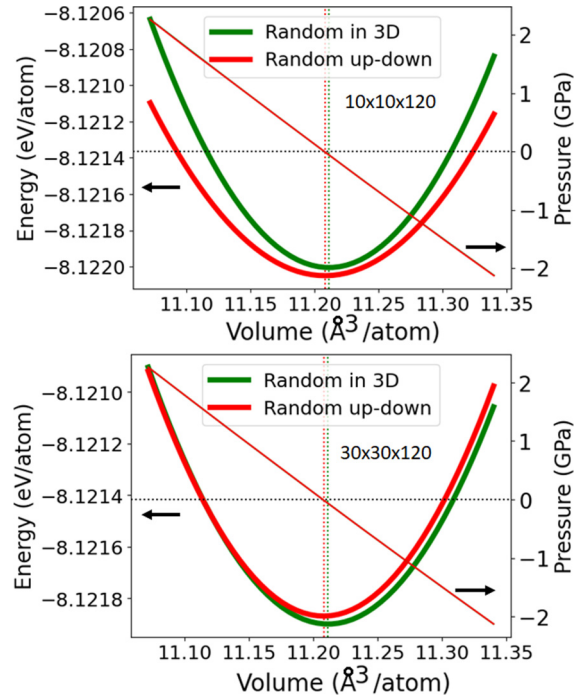

FIG. 4. Calculated equation of state of BCC Fe assuming two types of paramagnetic-like state: (green line) with randomly oriented magnetic moments along 3D directions, and (red line) random up-down orientations. Vertical dash line stands for the equilibrium volume V_0^r. The system size is (top) $10 \times 10 \times 120$ and (bottom) $30 \times 30 \times 120$ unit cells.

SOC interaction (dipole and quadrupole Néel's terms) in the spin-lattice model. In Fig. 4, we show the calculated EOS of BCC Fe at these paramagnetic-like states using system sizes $10 \times 10 \times 120$ and $30 \times 30 \times 120$ unit cells. We observe that increasing the system size up to $30 \times 30 \times 120$ gives similar EOS for both types of paramagnetic-like states, so that we use this size to calculate v^r through the method based on the oscillation of the kinetic energy. Moreover, since this system size is sufficiently large, we do not need to compute v^r for several random configurations and average them, or use special quasirandom structure (SQS) method [76]. Note that for the ferromagnetic state (parallel collinear spins) we do not need such a large size, so that we use a system size $10 \times 10 \times 120$ unit cells to compute v^c. In Fig. 5 we show the calculated kinetic energy versus time for BCC Fe at these two considered paramagnetic-like states. Here, we simulated three cases using an initial displacement amplitude $u_0 = 0.01a_0$, $u_0 = 0.05a_0$ and $u_0 = 0.1a_0$. We see that the paramagnetic-like state with randomly oriented magnetic moments along 3D directions increases the kinetic energy rapidly, so that it is not possible to fit this behavior to Eq. (11). This is due to the fact that this spin configuration corresponds to a thermal equilibrium state with spin temperature T_{spin} above $T_C = 1043K$ ($T_{\mathrm{spin}} > T_C$), hence the spin system interchanges energy with the phonon system, which is initially at zero temperature ($T_{\mathrm{ph}} = 0$ K), trying to equilibrate their temperatures [52]. Consequently, the lattice temperature increases rapidly, as seen in the dynamics of the kinetic energy. On the other hand, the configuration with random up-down spins is a paramagnetic-like state in terms

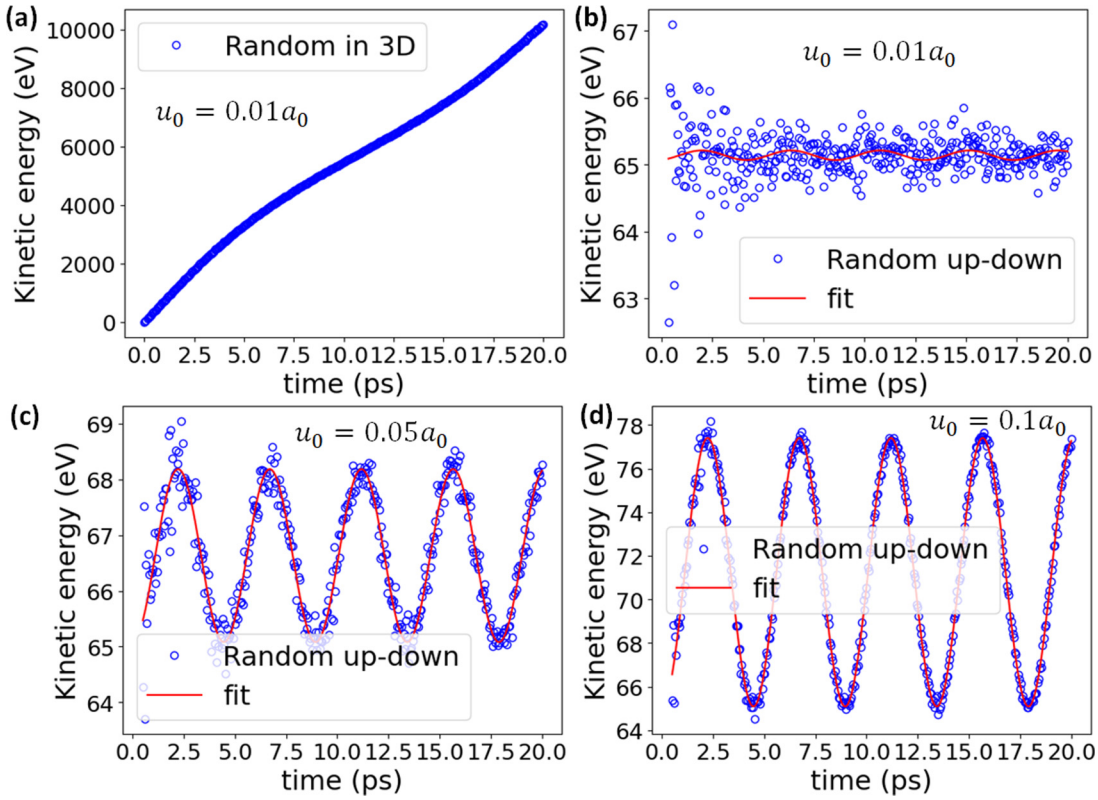

FIG. 5. Kinetic energy vs time of a transverse standing wave propagating in the direction $\boldsymbol{k} \parallel [001]$ with polarization $\boldsymbol{u} \parallel [100]$ for BCC Fe at paramagnetic-like states: (a) with randomly oriented magnetic moments along 3D directions and random up-down orientations using an initial displacement amplitude (b) $u_0 = 0.01a_0$, (c) $0.05a_0$, and (d) $0.1a_0$.

of the total energy but it does not correspond to a thermally equilibrated state above T_C. For example, the spin temperature for this state using the definition of Nurdin *et al.* [52,77] is $T_{\text{spin}} = 0$ K. Hence, it can mechanically stabilize the oscillation of the kinetic energy by introducing a small energy shift ($\sim$65 eV $= 0.3$ meV/atom) on the kinetic energy [Eq. (11)]. In this case, we can extract the frequency of the sound wave f^r (do not confuse with the measured frequency F in the pulse echo method) if the initial displacement amplitude u_0 is sufficiently large ($u_0 > 0.01a_0$) to overcome the noise fluctuations of the kinetic energy. From the fitting we obtain the frequency $f^r = 0.111619$ THz. We can estimate the sound velocity at the paramagnetic state by inserting the calculated f^r and $k^r = 2\pi/(120a_0^r)$ in Eq. (12), finding $v^r = 3776.4$ m/s. At the collinear state, we obtain the frequency $f^c = 0.106063$ THz. Hence, the estimated sound velocity using Eq. (12) is $v^c = 3602.2$ m/s. Consequently, using Eq. (12) leads to a fractional change in velocity $(v^c - v^r)/v^r = -0.0435$.

The FDM is a more rigorous and accurate approach to compute v^r than the oscillation of the kinetic energy since it has no problems associated with the spin-phonon stability for the paramagnetic-like states at zero temperature. Applying the methodology described in Sec. II C 2, the FDM gives $(v^c - v^r)/v^r = -0.048$ and -0.0408 for paramagnetic-like state with randomly oriented magnetic moments in 3D and randomly up-down orientations, respectively. Alternatively, we can also estimate it by using the corrections to elastic constants, as explained in Sec. II C 3 and Appendix A. For example, using the elastic constant C_{44}^r and density ρ^r at the paramagnetic state (see Table II) in Eq. (14) gives $v^r = 3807.9$ m/s, while for the collinear state we get $v^c = 3615.7$ m/s. This gives $(v^c - v^r)/v^r = -0.0505$. Therefore we see that the fractional change in velocity obtained with the three approaches (from the oscillation of the kinetic energy, FDM and corrections to elastic constants) are consistent with each other. Last, we can also estimate the isotropic morphic coefficient $m_3^{\alpha,2}$ by inserting the calculated sound velocities (v^r and v^c), equilibrium lattice parameters (a_0^r and a_0^c) and elastic constant C_{44}^c in Eq. (21). This procedure gives $m_3^{\alpha,2} = -60.8$ GPa using the velocities derived from the oscillation of the kinetic energy, and $m_3^{\alpha,2} = -66.5$ and -57.4 GPa with the FDM for paramagnetic-like state with randomly oriented magnetic moments in 3D and randomly up-down orientations, respectively, while using the velocities given by the corrections to the elastic constants we find $m_3^{\alpha,2} = -69.7$ GPa.

In the case of a longitudinal wave propagating along $\boldsymbol{k} \parallel [001]$ with polarization $\boldsymbol{u} \parallel [001]$, Eq. (19) reads [10]

$$\begin{aligned}
\left.\frac{v^c - v^r}{v^r}\right|_{\boldsymbol{u}\parallel[001]}^{\boldsymbol{k}\parallel[001]} &= \left.\frac{F^c - F^r}{F^r}\right|_{\boldsymbol{u}\parallel[001]}^{\boldsymbol{k}\parallel[001]} + \left.\frac{l^c - l^r}{l^r}\right|^{\boldsymbol{k}\parallel[001]}, \\
\left.\frac{F^c - F^r}{F^r}\right|_{\boldsymbol{u}\parallel[001]}^{\boldsymbol{k}\parallel[001]} &= Y\left(m_i^{\alpha,2}\right)\Big|_{\boldsymbol{u}\parallel[001]}^{\boldsymbol{k}\parallel[001]} = \frac{m_1^{\alpha,2}}{3C_{11}^c}, \\
\left.\frac{l^c - l^r}{l^r}\right|^{\boldsymbol{k}\parallel[001]} &= \frac{a_0^c - a_0^r}{a_0^r},
\end{aligned} \tag{22}$$

TABLE III. Calculated isotropic morphic coefficients of a wave propagating along $\boldsymbol{k} \parallel [001]$ using the spin-lattice model of BCC Fe without SOC.

Method	$\boldsymbol{u}$	Paramagnetic State	Morphic coefficient	GPa
Kinetic energy	$\boldsymbol{u} \parallel [100]$	Random in 3D	$m_3^{\alpha,2}$	–
		Random up-down		−60.8
FDM		Random in 3D		−66.5
		Random up-down		−57.4
Elastic constants		Random in 3D		−69.7
Kinetic energy	$\boldsymbol{u} \parallel [001]$	Random in 3D	$m_1^{\alpha,2}$	–
		Random up-down		–
FDM		Random in 3D		−10.6
		Random up-down		−8.0
Elastic constants		Random in 3D		−4.6

where $m_1^{\alpha,2}$ is an isotropic morphic coefficient defined in Eq. (B10). Following the same procedure as before and using Eq. (22), we find $m_1^{\alpha,2} = -10.6$ and -8.0 GPa through the FDM for paramagnetic-like state with randomly oriented magnetic moments in 3D and randomly up-down orientations, respectively, and $m_1^{\alpha,2} = -4.6$ GPa via the corrections to the elastic constants. Unfortunately, for the simulated cases of the longitudinal mode, the oscillation of the kinetic energy was not sufficiently stable to extract the frequency at the paramagnetic-like state (f^r), so that we could not estimate $m_1^{\alpha,2}$ with this approach. In Table III, we present a summary of the results obtained for the two isotropic morphic coefficients of BCC Fe calculated in this work. We point out that the elastic constants at the paramagnetic state (C_{ij}^r) and the isotropic morphic coefficients (m^α) are sensitive to the volume magnetostriction ω_S of the spin-lattice model.

B. Anisotropic magnetoelastic effects

For the analysis of anisotropic effects, we follow the same procedure, but now we switch on the SOC (dipole and quadrupole Néel's terms) in order to compute the velocity $v^{\rm SOC}$. We first consider a transverse wave propagating along $\boldsymbol{k} \parallel [001]$ with polarization $\boldsymbol{u} \parallel [100]$ and magnetization $\boldsymbol{M} \perp [001]$. In this case, the functions in Eq. (20) read [11]

$$
\begin{aligned}
G\Big|_{\boldsymbol{u}\parallel[100]}^{\boldsymbol{k}\parallel[001]\perp\boldsymbol{M}} &= \frac{m_3^{\gamma,2}}{8C_{44}^c}\left(\frac{1}{3} - \cos 2\phi\right),\\
R\Big|_{\boldsymbol{u}\parallel[100]}^{\boldsymbol{k}\parallel[001]\perp\boldsymbol{M}} &= \frac{1}{2}(\lambda^{\gamma,2} - \lambda^{\varepsilon,2})[1+\cos 2\phi]\\
&= \frac{3}{4}(\lambda_{001} - \lambda_{111})[1+\cos 2\phi],\\
S\Big|_{\boldsymbol{u}\parallel[100]}^{\boldsymbol{k}\parallel[001]\perp\boldsymbol{M}} &= -\frac{(B^{\varepsilon,2})^2(1+\cos 2\phi)}{4C_{44}^c\mu_0 M_s\left(H+M_s+H_D+\frac{K_1[3+\cos 4\phi]}{2\mu_0 M_s}\right)},\\
H &\gg \frac{2K_1}{\mu_0 M_s},\\
\frac{l^{\rm SOC}-l^c}{l^c}\Big|^{\boldsymbol{k}\parallel[001]\perp\boldsymbol{M}} &= -\frac{1}{3}\lambda^{\gamma,2} = -\frac{1}{2}\lambda_{001},
\end{aligned}
\tag{23}
$$

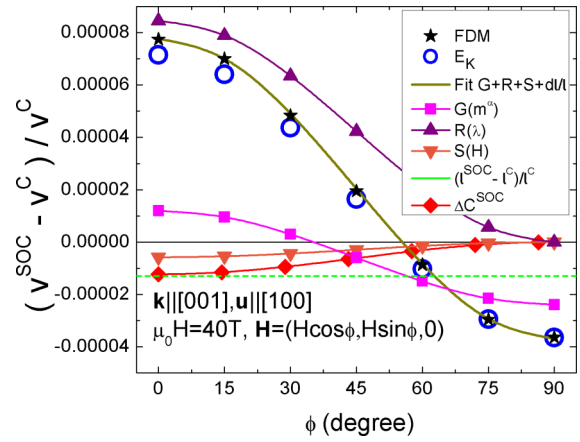

FIG. 6. Fractional change in velocity of BCC Fe vs the direction of the applied magnetic field $\boldsymbol{H} = (H\cos\phi, H\sin\phi, 0)$ on the plane XY for transverse wave propagating along $\boldsymbol{k} \parallel [001]$ with polarization $\boldsymbol{u} \parallel [100]$. The magnitude of the applied field is $\mu_0 H = 40$ T. Black stars represent the calculations with spin-lattice simulations obtained from the FDM, while brown solid line is the fitting of these data to the summation of functions G, R, S, and $(l^{\rm SOC} - l^c)/l^c$ in Eq. (23). Blue circles stand for the calculations with spin-lattice simulations obtained from the oscillation of the kinetic energy (E_K). Each function G, R, S, and $(l^{\rm SOC} - l^c)/l^c$ in Eq. (23) is plotted with pink squares, purple triangles, orange triangles and green dash line, respectively. Red diamonds correspond to the calculations using the corrections to the elastic constants given by Eq. (A22).

where ϕ is the angle between $\boldsymbol{M}$ and crystallographic direction [100] and H_D is the demagnetizing field. In our simulations, $H_D = 0$ since we do not include dipole-dipole interactions. The MEL constant $B^{\varepsilon,2} = b_2$ and magnetostrictive coefficients $\lambda^{\gamma,2} = 3\lambda_{001}/2$ and $\lambda^{\varepsilon,2} = 3\lambda_{111}/2$ are defined in Appendix B. The form of function G is the same as in Ref. [10], but note that it is not the same as in Ref. [1] due to a different definition of morphic coefficients and high-order MEL constants. The fractional change in length along [001] is obtained from the anisotropic part of Eq. (B8). The fractional change in velocity obtained from the oscillation of the kinetic energy and the FDM for the spin-lattice model of BCC Fe is shown in Fig. 6. It is performed at high applied magnetic field $\mu_0 H = 40$ T where $\boldsymbol{H} \parallel \boldsymbol{M}$. In analogy to experiment, we extract the morphic coefficient $m_3^{\gamma,2}$ by fitting the results given by the spin-lattice simulations to the summation of functions G, R, S and $(l^{\rm SOC} - l^c)/l^c$ in Eq. (23). Here, all materials parameters in these functions are constrained to corresponding values of the spin-lattice model (see Table II), except $m_3^{\gamma,2}$ which is a fitting parameter. This procedure gives $m_3^{\gamma,2} = -14.3$ MPa for method based on the oscillation of the kinetic energy, and $m_3^{\gamma,2} = -15.3$ MPa using the FDM. In Fig. 6, we also calculated the fractional change in velocity using the corrections to the elastic constants given by Eq. (A22). We see that this approach gives similar results to the field-dependent function $S(H)$, since the linear MEL theory (which does not include high-order MEL terms) was used both by Simon [15] to derive function $S(H)$ and Rinaldi *et al.* [18] to obtain the SOC corrections ($\triangle C^{\rm SOC}$) to the elastic constants [1].

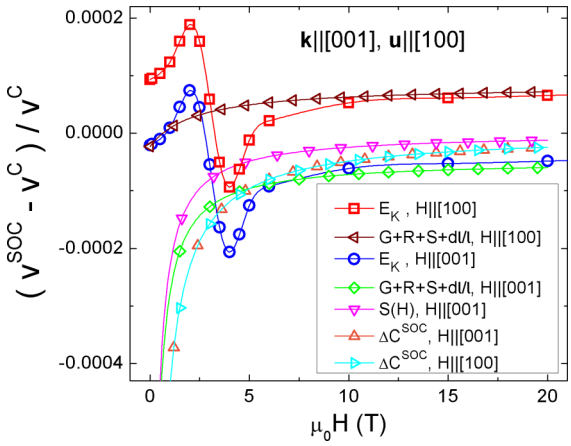

FIG. 7. Fractional change in velocity of BCC Fe vs the magnitude of the applied magnetic field along $\boldsymbol{H} \parallel [100]$ and $\boldsymbol{H} \parallel [001]$ for a transverse wave propagating along $\boldsymbol{k} \parallel [001]$ with polarization $\boldsymbol{u} \parallel [100]$. Blue points and red squares stand for the calculations with spin-lattice simulations obtained from the oscillation of the kinetic energy for the cases $\boldsymbol{H} \parallel [100]$ and $\boldsymbol{H} \parallel [001]$, respectively. Brown triangles and green diamonds correspond to the summation of functions G, R, S and $(l^{\mathrm{SOC}} - l^c)/l^c$ in Eqs. (23) and (24) for the cases $\boldsymbol{H} \parallel [100]$ and $\boldsymbol{H} \parallel [001]$, respectively. The function $S(H)$ in Eq. (24) is plotted with pink triangles. Orange and cyan triangles represent the calculations using the corrections to the elastic constants given by Eq. (A22).

The case of a transverse wave propagating along $\boldsymbol{k} \parallel [001]$ with polarization $\boldsymbol{u} \parallel [100]$ and magnetization $\boldsymbol{M} \parallel [100]$ is a particular case of Eq. (24) when $\phi = 0$. This case is calculated using the spin-lattice model for different values of the applied field in Fig. 7. Here, we also plot the case when the magnetization is $\boldsymbol{M} \parallel [001]$, where the functions in Eq. (20) now read [11]

$$
\begin{aligned}
G\Big|_{\boldsymbol{u}\parallel[100]}^{\boldsymbol{k}\parallel\boldsymbol{M}\parallel[001]} &= -\frac{m_3^{\gamma,2}}{12C_{44}^c}, \\
R\Big|_{\boldsymbol{u}\parallel[100]}^{\boldsymbol{k}\parallel\boldsymbol{M}\parallel[001]} &= \lambda^{\varepsilon,2} - \lambda^{\gamma,2} = \frac{3}{2}(\lambda_{111} - \lambda_{001}), \\
S\Big|_{\boldsymbol{u}\parallel[100]}^{\boldsymbol{k}\parallel\boldsymbol{M}\parallel[001]} &= -\frac{(B^{\varepsilon,2})^2}{2C_{44}^c\mu_0 M_s\left(H + H_D + \frac{2K_1}{\mu_0 M_s}\right)}, \\
& H \gg \frac{2K_1}{\mu_0 M_s}, \\
\frac{l^{\mathrm{SOC}} - l^c}{l^c}\Big|^{\boldsymbol{k}\parallel\boldsymbol{M}\parallel[001]} &= \frac{2}{3}\lambda^{\gamma,2} = \lambda_{001},
\end{aligned}
\tag{24}
$$

In Fig. 7, we see that both calculated cases ($\boldsymbol{M} \parallel [100]$ and $\boldsymbol{M} \parallel [001]$) are in good agreement with the theory at high applied magnetic fields ($\mu_0 H > 5$ T). In this figure, we used the previously calculated value $m_3^{\gamma,2} = -14.3$ MPa derived from the oscillation of the kinetic energy in order to plot the theoretical function G, while for the other parameters in Eqs. (23) and (24), we set the values of the spin-lattice model (see Table II). We also see that the spin-lattice model can correctly reproduce the rotational-magnetostrictive effect at high applied magnetic fields predicted by Eqs. (23) and (24), that is

$$
\begin{aligned}
&\lim_{H\to\infty}\left[\frac{v^{\mathrm{SOC}} - v^c}{v^c}\Big|_{\boldsymbol{u}\parallel\boldsymbol{M}\parallel[100]}^{\boldsymbol{k}\parallel[001]} - \frac{v^{\mathrm{SOC}} - v^c}{v^c}\Big|_{\boldsymbol{u}\parallel[100]}^{\boldsymbol{k}\parallel\boldsymbol{M}\parallel[001]}\right] \\
&= \left[R\Big|_{\boldsymbol{u}\parallel\boldsymbol{M}\parallel[100]}^{\boldsymbol{k}\parallel[001]} + \frac{l^{\mathrm{SOC}} - l^c}{l^c}\Big|_{\boldsymbol{M}\parallel[100]}^{\boldsymbol{k}\parallel[001]}\right] \\
&\quad - \left[R\Big|_{\boldsymbol{u}\parallel[100]}^{\boldsymbol{k}\parallel\boldsymbol{M}\parallel[001]} + \frac{l^{\mathrm{SOC}} - l^c}{l^c}\Big|^{\boldsymbol{k}\parallel\boldsymbol{M}\parallel[001]}\right] \\
&= 2(\lambda^{\gamma,2} - \lambda^{\varepsilon,2}) - \frac{3}{2}\lambda_{001} = \frac{3}{2}\lambda_{001} - 3\lambda_{111}.
\end{aligned}
\tag{25}
$$

The factor $2(\lambda^{\gamma,2} - \lambda^{\varepsilon,2})$ arises from the rotational-magnetostrictive effect in the fractional change in pulse echo frequency F, as shown in Refs. [1,10,11], while the additional factor $-3\lambda_{001}/2$ comes from the fractional change in length. The fractional change in velocity derived from the corrections to elastic constants [Eq. (A22)] approaches the field-dependent function $S(H)$ at high fields along $\boldsymbol{H} \parallel [001]$, but it does not reproduce the high-order effects since the used corrections to the elastic constants are based on the linear MEL theory [18]. The results from the spin-lattice simulations exhibit a nonmonotonic behavior at low applied magnetic fields ($\mu_0 H < 5$ T). Similar pattern has been experimentally observed in single cubic crystals of disordered Co-Pt alloy [11]. In this low-field regime, the anisotropy field ($\mu_0 H_K = 2K_1/M_s$) is comparable to the applied magnetic field ($H \sim H_K$). Hence, this behavior comes from an interplay between these two fields. More precisely, it is associated to the Δs effect [11], where stress anisotropy (K_σ) can arise from the stress originated by the propagation of ultrasonic pulses [78]. This stress anisotropy effect naturally emerges in the spin-lattice model through the quadrupole ($q(r_{ij})$) and dipole ($l(r_{ij})$) terms of the Néel energy in Eq. (2) due to the lattice deformation induced by the sound wave. For example, in Appendix C2, we analyze the anisotropy field induced by a static tetragonal deformation coming from the dipole term [Eq. (C8)]. The analysis of the stress anisotropy created by the sound wave is more complex than the static case since it becomes both time and spatial dependent as the wave is propagating through the material. Such analysis is not performed in the present work. Note that the low-field regime can not be described by the current theory since the field-dependent term $S(H)$ was derived by Simon only under the assumption of high applied magnetic fields [15] ($H \gg 2K_1/[\mu_0 M_s]$). Additionally, this regime is difficult to characterize in experiment since depends strongly on the remanent state [11]. Hence, we see that the spin-lattice simulations could be a useful tool to explore and understand the physics of MEL effects on sound velocity in this regime.

Let us now consider a longitudinal wave propagating along $\boldsymbol{k} \parallel [001]$ with polarization $\boldsymbol{u} \parallel [001]$. If the magnetization is along $\boldsymbol{M} \parallel [001]$, then functions in Eq. (20) read [11]

$$
\begin{aligned}
G\Big|_{\boldsymbol{u}\parallel[001]}^{\boldsymbol{k}\parallel[001]\parallel\boldsymbol{M}} &= \frac{2m_1^{\gamma,2}}{3C_{11}^c}, \\
R\Big|_{\boldsymbol{u}\parallel[001]}^{\boldsymbol{k}\parallel[001]\parallel\boldsymbol{M}} &= 0,
\end{aligned}
$$

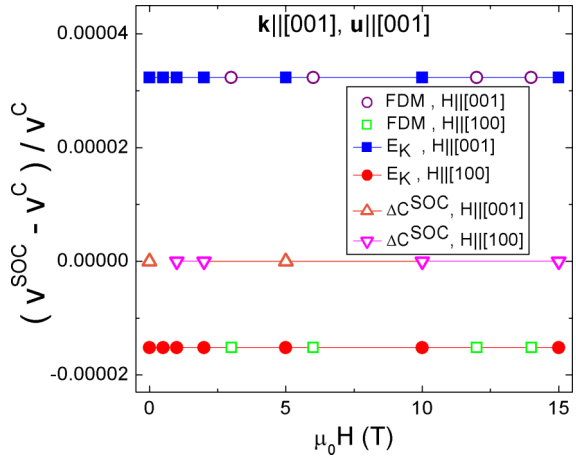

FIG. 8. Fractional change in velocity of BCC Fe vs the magnitude of the applied magnetic field along $\boldsymbol{H} \parallel [100]$ and $\boldsymbol{H} \parallel [001]$ for a longitudinal wave propagating along $\boldsymbol{k} \parallel [001]$ with polarization $\boldsymbol{u} \parallel [001]$. Open green squares and purple circles stand for the calculations with spin-lattice simulations obtained from the FDM for the cases $\boldsymbol{H} \parallel \boldsymbol{M} \parallel [100]$ and $\boldsymbol{H} \parallel \boldsymbol{M} \parallel [001]$, respectively. Red points and blue squares stand for the calculations with spin-lattice simulations obtained from the oscillation of the kinetic energy for the cases $\boldsymbol{H} \parallel \boldsymbol{M} \parallel [100]$ and $\boldsymbol{H} \parallel \boldsymbol{M} \parallel [001]$, respectively. Open orange and pink triangles represent the calculations using the corrections to the elastic constants given by Eq. (A24) for the cases $\boldsymbol{H} \parallel \boldsymbol{M} \parallel [100]$ and $\boldsymbol{H} \parallel \boldsymbol{M} \parallel [001]$, respectively.

$$S\Big|_{\boldsymbol{u}\parallel[001]}^{\boldsymbol{k}\parallel[001]\parallel\boldsymbol{M}} = 0,$$

$$\frac{l^{\mathrm{SOC}} - l^{c}}{l^{c}}\Big|_{\boldsymbol{u}\parallel[001]}^{\boldsymbol{k}\parallel[001]\parallel\boldsymbol{M}} = \frac{2}{3}\lambda^{\gamma,2} = \lambda_{001}, \tag{26}$$

while if the magnetization is along $\boldsymbol{M} \parallel [100]$, then we have [11]

$$\frac{v^{\mathrm{SOC}} - v^{c}}{v^{c}}\Big|_{\boldsymbol{u}\parallel[001]}^{\boldsymbol{k}\parallel[001],\boldsymbol{M}\parallel[100]} = -\frac{1}{2}\frac{v^{\mathrm{SOC}} - v^{c}}{v^{c}}\Big|_{\boldsymbol{u}\parallel[001]}^{\boldsymbol{k}\parallel\boldsymbol{M}\parallel[001]}. \tag{27}$$

We simulated these two cases for different values of the applied magnetic field in Fig. 8. The spin-lattice simulations give a constant fractional change in velocity as a function of the applied field, which is consistent with the lack of field dependency [$S(H) = 0$] in Eqs. (26) and (27). We also see that it correctly reproduces the relationship provided by Eq. (27), which comes from a high-order effect induced by the anisotropic morphic coefficient $m_1^{\gamma,2}$ via the function G and fractional change in length. We can derive the morphic coefficient $m_1^{\gamma,2}$ by fitting the summation of the functions in Eq. (26), where the values for C_{11}^{c} and λ_{001} are taken from Table II, to the fractional change in velocity given by the spin-lattice simulations in Fig. 8. This procedure gives $m_1^{\gamma,2} = 2.4$ MPa using both the FDM and the oscillation of the kinetic energy. The fractional change in velocity derived from the corrections to elastic constants [Eq. (A24)] is zero for both cases ($\boldsymbol{M} \parallel [001]$ and $\boldsymbol{M} \parallel [100]$) because $\triangle S_{33}^{\mathrm{SOC}}(H) = 0$, as expected from the fact that $S(H) = 0$ in Eq. (26).

In Table IV, we present a summary of the two anisotropic morphic coefficients derived for the spin-lattice model of BCC Fe in this work. There are in total nine morphic coefficients $m_i^{\mu,2}$ (where $\mu = \alpha, \beta, \gamma$ and $i = 1, 2, 3$) up to second order in the direction cosine of magnetization, see Appendix B [1,10,11]. Although some of these morphic coefficients were not computed in this study, they can be evaluated in a similar way by choosing other propagating directions of the wave [11]. In Tables III and IV, we see that the isotropic morphic coefficient $m_3^{\alpha,2}$ (induced by the exchange interaction) is about four orders of magnitude larger than the anisotropic ones. This result is in good agreement with morphic coefficients reported for FCC Ni, where similar differences were observed [1,19]. Note that the extrapolation of the calculated morphic coefficients with this spin-lattice model to experiment is not obvious because they are linear combinations of third order in strain elastic constants ($\tilde{C}_{ijk}$) and second order in strain MEL constants ($\tilde{M}_i^{\mu,2}$) [1,10,11]. The SNAP interatomic potential used in the model might describe, at least to some extent, experimental high-order elastic constants thanks to its quantum mechanical derivation and complex functional form [53,58]. However, it is not clear that the Néel model used in this work could be sufficiently accurate to describe correctly experimental high-order MEL constants $\tilde{M}_i^{\mu,2}$ since it was originally designed to reproduce the experimental MEL constants $B^{\mu,2}$ only up to first order in strain [54]. Possible deviations due to the Néel model might not be relevant in the calculation of those morphic coefficients where the contribution of high-order elastic constants is much greater than the high-order MEL constants [$\tilde{M}_i^{\mu,2} \ll \tilde{C}_{ljk}\lambda^{\mu,2}$, see Eq. (B10)] [11].

TABLE IV. Calculated anisotropic morphic coefficients of the spin-lattice model for BCC Fe.

Method	Morphic coefficient	MPa
Kinetic energy	$m_3^{\gamma,2}$	−14.3
FDM		−15.3
Kinetic energy	$m_1^{\gamma,2}$	2.4
FDM		2.4

C. Magnetoelastic effects on phonon dispersion

In previous sections, we studied the MEL effects on phonons with low momentum ($k_{\mathrm{ph}} \to 0$) in order to compare the atomistic simulations with the continuum theory of sound velocity in a solid. Here, we extend our study by calculating the MEL effects on the frequency of phonons with larger momentum. In particular, we compute the phonon dispersion along the Γ- H line of k points, see Fig. 9. In general, we observe small changes in phonon's frequency due to MEL effects. For comparison, we also plot in Fig. 9 the density-functional theory (DFT) calculations performed by Ikeda *et al.* [79] using SQS with size $2 \times 2 \times 2$. Close to the Γ point ($k_{\mathrm{ph}} \to 0$), our calculations with the spin-lattice model are very similar to the DFT results reported in Ref. [79]. However, at higher values of k, we obtain that the phonon frequencies of the paramagnetic state are slightly larger than in the ferromagnetic state, while the opposite behavior was found by Ikeda *et al.* [79] with also a higher shift in the

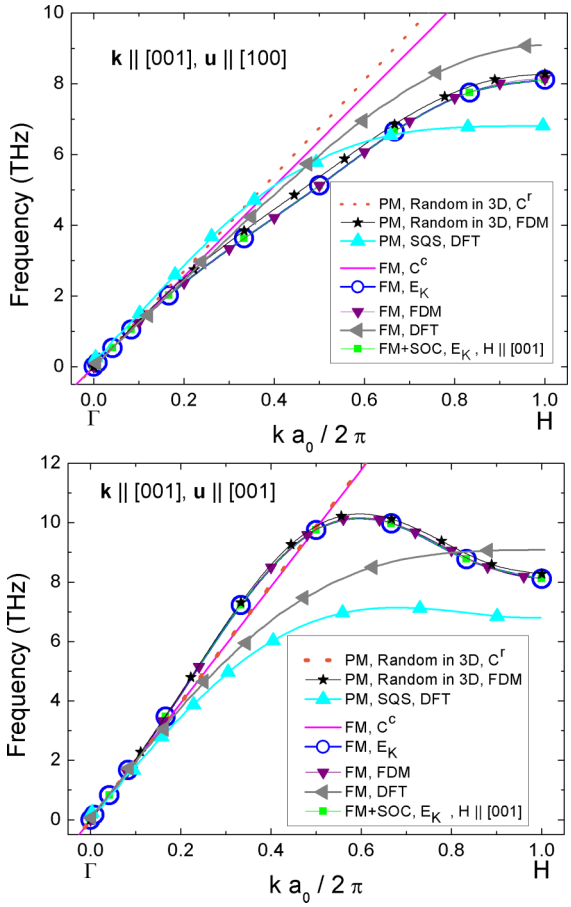

FIG. 9. Phonon dispersion of (top) transverse and (bottom) longitudinal modes. Black stars correspond to calculations with the FDM at paramagnetic (PM) state with randomly oriented magnetic moments in 3D. Dash orange and solid pink lines stand for the calculations with the elastic constants at the PM and ferromagnetic collinear without SOC states (FM), respectively. Blue circles and violet triangles show data from the oscillation of the kinetic energy and FDM at a collinear state without SOC, respectively. Green squares represent calculations obtained from the oscillation of the kinetic energy at a collinear state with SOC under an applied magnetic field $\mu_0 \boldsymbol{H} = (0, 0, 40)$ T. Cyan and grey triangles give DFT calculations performed by Ikeda *et al.* [79] using SQS for the PM and FM states, respectively.

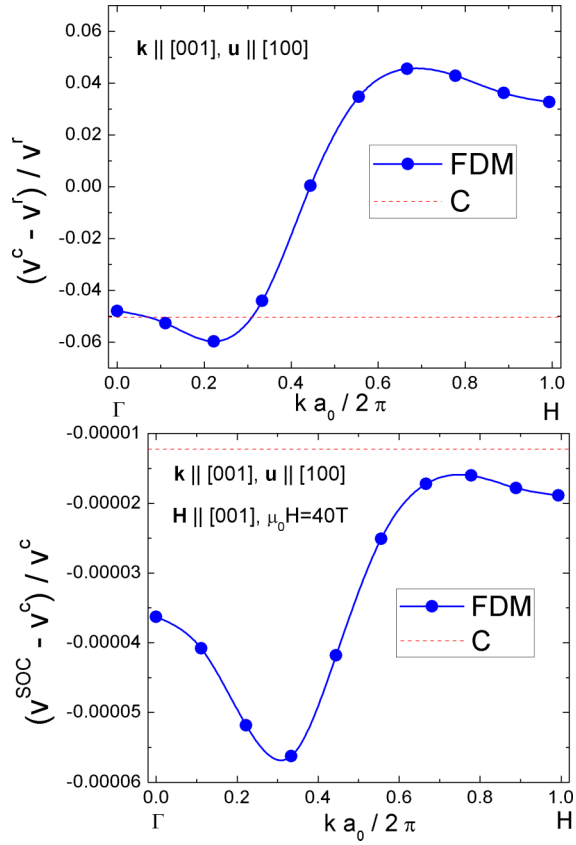

FIG. 10. Fractional change in group velocity of phonons vs phonon's momentum along $\boldsymbol{k}$ || [001] with polarization $\boldsymbol{u}$ || [100]. (Top) Fractional change in velocity of the collinear state (including only exchange interaction) with respect to the paramagnetic state with randomly oriented magnetic moments in 3D. (Bottom) Fractional change in velocity of the collinear state (including both exchange interaction and SOC) with respect to collinear state including only exchange interaction. The calculations are performed using the FDM. Red dash line represents the calculation with the corrections to the elastic constants given by Eqs. (A21) and (A22).

frequencies. Similar results as in Ref. [79] have been reported by Novikov *et al.* [80] using DFT and magnetic moment tensor potentials. In Fig. 10, we analyze how the fractional change in the phonon group velocity is influenced by the magnitude of phonon momentum $k_{\rm ph}$. We observe a significant modification of $(v^c - v^r)/v^r$ as we increase $k_{\rm ph}$, where the sign is changed in the middle of Γ-H line. This result suggests that the theoretical equation derived for sound waves Eq. (21) might only hold for phonon with low momentum ($k_{\rm ph} \to 0$). On the other hand, $(v^{\rm SOC} - v^c)/v^c$ is not so strongly affected by the magnitude of phonon momentum, which means that in some cases the theoretical fractional change in velocity derived for sound waves might still provide at least a reasonable qualitative description for phonons with larger momentum.

As shown in Appendix A, the continuum mechanics within the infinitesimal strain theory (corrections to elastic constants) gives a linear dependence of the frequency f on the wave vector k [see, for example, Eq. (A13)]. In Fig. 9, we see that this description is correct for low values of the wave vector ($ka_0/2\pi < 0.1$). At higher values of the wave vector ($ka_0/2\pi > 0.1$), quantum mechanics and classical atomistic simulations provide a more realistic relationship between the frequency f and wave vector k than continuum mechanics. Similarly, in Fig. 10, the continuum mechanics gives a fractional change in sound velocity that does not depend on the wave vector k [see Eqs. (A21)–(A24)], which again would be a good approximation for low values of the wave vector ($ka_0/2\pi < 0.1$). Note that the deviation between atomistic and continuum mechanics observed in $(v^{\rm SOC} - v^c)/v^c$ at low values of the wave vector ($ka_0/2\pi < 0.1$) is due to the used corrections to elastic constants $\Delta C^{\rm SOC}$, which only account for the field-dependent term $S(H)$ (Simon effect). This deviation can be also observed in Fig. 7 at high applied magnetic fields. Concerning $(v^c - v^r)/v^r$, we point out that our

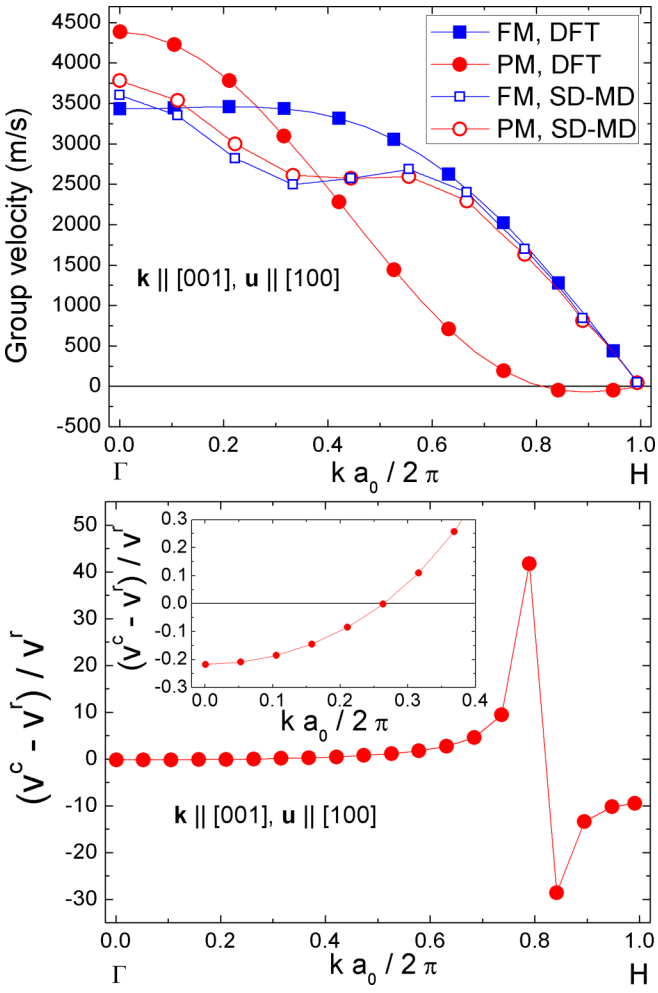

FIG. 11. (Top) Group velocity of phonons vs phonon's momentum along $\boldsymbol{k} \parallel [001]$ with polarization $\boldsymbol{u} \parallel [100]$ at ferromagnetic (FM, v^c) and paramagnetic (PM, v^r) state calculated with (solid symbols) DFT and (open symbols) SD-MD. (Bottom) Fractional change in group velocity of the collinear state (including only exchange interaction) with respect to the PM state given by DFT calculation. In the inset we zoom in the low phonon momentum regime ($ka_0/2\pi < 0.4$). The DFT calculation was obtained by reproducing the work done by Ikeda *et al.* [79] using SQS within the FDM.

atomsitic model could give significant different results as DFT [79] at high values of the wave vector ($ka_0/2\pi > 0.5$) due to the deviation observed in phonon's dispersion (Fig. 9). This fact is illustrated in Fig. 11, which should be compared with the results given by the atomsitic model in Fig. 10. A better a agreement with DFT might be achieved by using magnetic momentum tensor potentials in the atomistic spin-lattice models [80]. Note also that the approximation $(v^c - v^r)/v^r \ll 1$ used in Eq. (15) is fulfilled by our classical spin-lattice model (see Fig. 10) for all simulated k values but not by the DFT calculation [79] (see Fig. 11).

V. CONCLUSIONS

In summary, we found that classical atomistic spin-lattice simulations based on the Néel model can describe the main four MEL effects on sound velocity (isotropic exchange effects, anisotropic morphic effects, field dependent effects and rotational-magnetostrictive effects). We verified this capability for a spin-lattice model of BCC Fe through three independent approaches: (i) analysis of the kinetic energy, (ii) forces, and (iii) corrections to elastic constants.

In analogy to experiment, we showed that the morphic coefficients (which are linear combination of high-order elastic and MEL constants) of the spin-lattice models can be derived from the analysis of the fractional change in velocity. The calculated morphic coefficients for the model of BCC Fe exhibit similar order of magnitude as in FCC Ni [1,19]. In the low magnetic field regime, our simulations revealed an interesting nonmonotonic dependence on the applied field of the fractional change in sound velocity associated with the Δs effect [11,78], which cannot be described by Simon's theory since it is valid only at high applied fields [15]. Hence, the presented computational framework could be a useful tool to explore and understand the field regimes still uncovered by the theory. In the analysis of MEL effects on phonon dispersion, we identified significant discrepancies between our spin-lattice model and DFT calculations [79] for high values of the wave vector k, which might be improved by using magnetic momentum tensor potentials in the atomistic models [80].

In the presented model, we restricted our analysis to zero-temperature and fixed magnitude of magnetic moments [81], which might be further extended in the future. As a complementary tool to quantum and continuum mechanics methods [30,43], we believe that classical spin-lattice simulations could be helpful to study the combination of magnetic and atomistic scale effects (e.g., vacancies, impurities, complex defects, or nanostructures) on sound velocity within a multi-scale approach. Similarly, we envisage that these atomistic models might also be exploited in the design of novel technological magnetoacoustic applications, such as acoustically assisted magnetic recording [32], by using them to find the optimal conditions for magnetization switching induced by acoustic waves.

ACKNOWLEDGMENTS

This work was supported by the ERDF in the IT4Innovations national supercomputing center - path to exascale project (CZ.02.1.01/0.0/0.0/16-013/0001791) within the OPRDE and projects "e-INFRA CZ (ID:90140)" and Donau No. 8X20050 by The Ministry of Education, Youth and Sports of the Czech Republic. This project has received funding from the European Union's Horizon 2020 research and innovation programme under Grant Agreement No 863155. S. Nikolov is an employee of Sandia National Laboratories, a multimission laboratory managed and operated by National Technology and Engineering Solutions of Sandia, LLC, a wholly owned subsidiary of Honeywell International Inc., for the U.S. Department of Energy's National Nuclear Security Administration under Contract No. DE-NA0003525. This paper describes objective technical results and analysis. Any subjective views or opinions that might be expressed in the paper do not necessarily represent the views of the U.S. Department of Energy or the United States Government. A. Fraile is

funded through the Sêr Cymru II 80761-BU-103 project by Welsh European Funding Office (WEFO) under the European Development Fund (ERDF).

APPENDIX A: MAGNETOELASTIC EFFECTS ON SOUND VELOCITY AS CORRECTIONS TO THE ELASTIC CONSTANTS

MEL effects on sound velocity can be described in terms of effective elastic constants. In this Appendix, we present a brief review of this approach. Let us start by deriving the general procedure to find the sound velocity in terms of the elastic constants. The equation of motion of an elastic wave is given by [82]

$$\rho \frac{\partial^2 u_i}{\partial t^2} = \sum_{j=x,y,z} \frac{\partial \sigma_{ij}}{\partial r_j}, \qquad i = x,\ y,\ \text{and}\ z, \tag{A1}$$

where ρ is the mass density, $\boldsymbol{u}$ is the displacement vector and σ_{ij} is the stress tensor that is related to the fourth-order elastic stiffness tensor c_{ijkl} and the second-order strain tensor ε_{ij} through the generalized Hooke's law

$$\sigma_{ij} = \sum_{k,l=x,y,z} c_{ijkl}\varepsilon_{kl}, \quad i, j = x,\ y,\ \text{and}\ z. \tag{A2}$$

Using the symmetry of the stress and strain tensors, the Hooke's law can be written in matrix notation as

$$\begin{pmatrix} \sigma_{xx} \\ \sigma_{yy} \\ \sigma_{zz} \\ \sigma_{yz} \\ \sigma_{zx} \\ \sigma_{xy} \end{pmatrix} = \begin{pmatrix} c_{xxxx} & c_{xxyy} & c_{xxzz} & c_{xxyz} & c_{xxzx} & c_{xxxy} \\ c_{yyxx} & c_{yyyy} & c_{yyzz} & c_{yyyz} & c_{yyzx} & c_{yyxy} \\ c_{zzxx} & c_{zzyy} & c_{zzzz} & c_{zzyz} & c_{zzzx} & c_{zzxy} \\ c_{yzxx} & c_{yzyy} & c_{yzzz} & c_{yzyz} & c_{yzzx} & c_{yzxy} \\ c_{zxxx} & c_{zxyy} & c_{zxzz} & c_{zxyz} & c_{zxzx} & c_{zxxy} \\ c_{xyxx} & c_{xyyy} & c_{xyzz} & c_{xyyz} & c_{xyzx} & c_{xyxy} \end{pmatrix} \begin{pmatrix} \varepsilon_{xx} \\ \varepsilon_{yy} \\ \varepsilon_{zz} \\ 2\varepsilon_{yz} \\ 2\varepsilon_{zx} \\ 2\varepsilon_{xy} \end{pmatrix}. \tag{A3}$$

To facilitate the manipulation of this equation it is convenient to define the following six-dimensional vectors (Voigt notation)

$$\tilde{\boldsymbol{\sigma}} = \begin{pmatrix} \tilde{\sigma}_1 \\ \tilde{\sigma}_2 \\ \tilde{\sigma}_3 \\ \tilde{\sigma}_4 \\ \tilde{\sigma}_5 \\ \tilde{\sigma}_6 \end{pmatrix} = \begin{pmatrix} \sigma_{xx} \\ \sigma_{yy} \\ \sigma_{zz} \\ \sigma_{yz} \\ \sigma_{zx} \\ \sigma_{xy} \end{pmatrix}, \qquad \tilde{\boldsymbol{\varepsilon}} = \begin{pmatrix} \tilde{\varepsilon}_1 \\ \tilde{\varepsilon}_2 \\ \tilde{\varepsilon}_3 \\ \tilde{\varepsilon}_4 \\ \tilde{\varepsilon}_5 \\ \tilde{\varepsilon}_6 \end{pmatrix} = \begin{pmatrix} \varepsilon_{xx} \\ \varepsilon_{yy} \\ \varepsilon_{zz} \\ 2\varepsilon_{yz} \\ 2\varepsilon_{zx} \\ 2\varepsilon_{xy} \end{pmatrix}, \tag{A4}$$

and replace c_{ijkl} by C_{nm} contracting a pair of cartesian indices into a single integer: $xx \to 1$, $yy \to 2$, $zz \to 3$, $yz \to 4$, $zx \to 5$, and $xy \to 6$. Using these conversion rules the Hooke's law is simplified to

$$\tilde{\sigma}_i = \sum_{j=1}^{6} C_{ij}\tilde{\varepsilon}_j, \quad i = 1, \ldots, 6 \tag{A5}$$

where in matrix form reads

$$\begin{pmatrix} \tilde{\sigma}_1 \\ \tilde{\sigma}_2 \\ \tilde{\sigma}_3 \\ \tilde{\sigma}_4 \\ \tilde{\sigma}_5 \\ \tilde{\sigma}_6 \end{pmatrix} = \begin{pmatrix} C_{11} & C_{12} & C_{13} & C_{14} & C_{15} & C_{16} \\ C_{21} & C_{22} & C_{23} & C_{24} & C_{25} & C_{26} \\ C_{31} & C_{32} & C_{33} & C_{34} & C_{35} & C_{36} \\ C_{41} & C_{42} & C_{43} & C_{44} & C_{45} & C_{46} \\ C_{51} & C_{52} & C_{53} & C_{54} & C_{55} & C_{56} \\ C_{61} & C_{62} & C_{63} & C_{64} & C_{65} & C_{66} \end{pmatrix} \begin{pmatrix} \tilde{\varepsilon}_1 \\ \tilde{\varepsilon}_2 \\ \tilde{\varepsilon}_3 \\ \tilde{\varepsilon}_4 \\ \tilde{\varepsilon}_5 \\ \tilde{\varepsilon}_6 \end{pmatrix}. \tag{A6}$$

We additionally assume that our material is hyperelastic (there exists an elastic energy function) what implies that $C_{ij} = C_{ji}$. Next, using Eqs. (A4) and (A5) in the equation of motion Eq. (A1) gives

$$\begin{aligned} \frac{\partial^2 u_x}{\partial t^2} &= \sum_{i=1}^{6} \left(C_{1i}\frac{\partial}{\partial r_x} + C_{6i}\frac{\partial}{\partial r_y} + C_{5i}\frac{\partial}{\partial r_z} \right)\tilde{\varepsilon}_i, \\ \frac{\partial^2 u_y}{\partial t^2} &= \sum_{i=1}^{6} \left(C_{6i}\frac{\partial}{\partial r_x} + C_{2i}\frac{\partial}{\partial r_y} + C_{4i}\frac{\partial}{\partial r_z} \right)\tilde{\varepsilon}_i, \\ \frac{\partial^2 u_z}{\partial t^2} &= \sum_{i=1}^{6} \left(C_{5i}\frac{\partial}{\partial r_x} + C_{4i}\frac{\partial}{\partial r_y} + C_{3i}\frac{\partial}{\partial r_z} \right)\tilde{\varepsilon}_i. \end{aligned} \tag{A7}$$

For small deformations (infinitesimal strain theory), the strain tensor can be expressed in terms of the displacement vector $\boldsymbol{u}$ as [82]

$$\varepsilon_{ij} = \frac{1}{2}\left(\frac{\partial u_i}{\partial r_j} + \frac{\partial u_j}{\partial r_i} \right), \qquad i, j = x,\ y,\ \text{and}\ z. \tag{A8}$$

Hence, combining this equation with Eq. (A4), the six-dimensional vector $\tilde{\varepsilon}_i$ can be expressed in terms of the displacement vector as

$$\tilde{\boldsymbol{\varepsilon}} = \begin{pmatrix} \tilde{\varepsilon}_1 \\ \tilde{\varepsilon}_2 \\ \tilde{\varepsilon}_3 \\ \tilde{\varepsilon}_4 \\ \tilde{\varepsilon}_5 \\ \tilde{\varepsilon}_6 \end{pmatrix} = \begin{pmatrix} \varepsilon_{xx} \\ \varepsilon_{yy} \\ \varepsilon_{zz} \\ 2\varepsilon_{yz} \\ 2\varepsilon_{zx} \\ 2\varepsilon_{xy} \end{pmatrix} = \begin{pmatrix} \frac{\partial u_x}{\partial r_x} \\ \frac{\partial u_y}{\partial r_y} \\ \frac{\partial u_z}{\partial r_z} \\ \frac{\partial u_y}{\partial r_z} + \frac{\partial u_z}{\partial r_y} \\ \frac{\partial u_x}{\partial r_z} + \frac{\partial u_z}{\partial r_x} \\ \frac{\partial u_x}{\partial r_y} + \frac{\partial u_y}{\partial r_x} \end{pmatrix}. \tag{A9}$$

Last, replacing Eqs. (A9) in Eq. (A7) and considering a monochromatic elastic wave $u_i = u_{0,i}e^{i(\boldsymbol{k}\cdot\boldsymbol{r}+2\pi ft)}$, we find [82]

$$\begin{pmatrix} A_{xx} & A_{xy} & A_{xz} \\ A_{yx} & A_{yy} & A_{yz} \\ A_{zx} & A_{zy} & A_{zz} \end{pmatrix} \cdot \begin{pmatrix} u_x \\ u_y \\ u_z \end{pmatrix} = \begin{pmatrix} 0 \\ 0 \\ 0 \end{pmatrix}, \tag{A10}$$

where

$$\begin{aligned}
A_{xx} &= -\rho(2\pi f)^2 + (k_xC_{11} + k_yC_{61} + k_zC_{51})k_x \\
&\quad + (C_{15}k_x + C_{65}k_y + C_{55}k_z)k_z \\
&\quad + (k_xC_{16} + k_yC_{66} + k_zC_{56})k_y, \\
A_{xy} &= (C_{14}k_x + C_{64}k_y + C_{54}k_z)k_z + (k_xC_{12} + k_yC_{62} + k_zC_{52})k_y \\
&\quad + (C_{16}k_x + C_{66}k_y + C_{56}k_z)k_x, \\
A_{xz} &= (C_{14}k_x + C_{64}k_y + C_{54}k_z)k_y + (C_{15}k_x + C_{65}k_y + C_{55}k_z)k_x \\
&\quad + (C_{13}k_x + C_{63}k_y + C_{53}k_z)k_z, \\
A_{yx} &= (k_xC_{61} + k_yC_{21} + k_zC_{41})k_x + (C_{65}k_x + C_{25}k_y + C_{45}k_z)k_z \\
&\quad + (k_xC_{66} + k_yC_{26} + k_zC_{46})k_y, \\
A_{yy} &= -\rho(2\pi f)^2 + (C_{64}k_x + C_{24}k_y + C_{44}k_z)k_z \\
&\quad + (k_xC_{62} + k_yC_{22} + k_zC_{42})k_y \\
&\quad + (C_{66}k_x + C_{26}k_y + C_{46}k_z)k_x, \\
A_{yz} &= (C_{64}k_x + C_{24}k_y + C_{44}k_z)k_y + (C_{65}k_x + C_{25}k_y + C_{45}k_z)k_x \\
&\quad + (C_{63}k_x + C_{23}k_y + C_{43}k_z)k_z, \\
A_{zx} &= (k_xC_{51} + k_yC_{41} + k_zC_{31})k_x + (C_{55}k_x + C_{45}k_y + C_{35}k_z)k_z \\
&\quad + (k_xC_{56} + k_yC_{46} + k_zC_{36})k_y, \\
A_{zy} &= (C_{54}k_x + C_{44}k_y + C_{34}k_z)k_z + (k_xC_{52} + k_yC_{42} + k_zC_{32})k_y \\
&\quad + (C_{56}k_x + C_{46}k_y + C_{36}k_z)k_x, \\
A_{zz} &= -\rho(2\pi f)^2 + (C_{54}k_x + C_{44}k_y + C_{34}k_z)k_y \\
&\quad + (C_{55}k_x + C_{45}k_y + C_{35}k_z)k_x \\
&\quad + (C_{53}k_x + C_{43}k_y + C_{33}k_z)k_z.
\end{aligned} \tag{A11}$$

From Eq. (A10), one can straightforwardly derive the sound velocity. For example, in the case of a transverse wave propagating along $\boldsymbol{k} \parallel [001]$ ($k_x = 0$ and $k_y = 0$) with polarization $\boldsymbol{u} \parallel [100]$ ($u_y = 0$ and $u_z = 0$), we obtain the following relation from Eq. (A10):

$$\left[-\rho(2\pi f)^2 + C_{55}k_z^2\right]u_x = 0, \tag{A12}$$

hence in this case, the frequency f is related to the wave vector $\boldsymbol{k}$ as

$$2\pi f(\boldsymbol{k})\Big|_{\boldsymbol{u}\parallel[100]}^{\boldsymbol{k}\parallel[001]} = k_z\sqrt{\frac{C_{55}}{\rho}}. \tag{A13}$$

The velocity of propagation of the wave (group velocity) $\boldsymbol{v}$ is given by the derivative of the frequency $2\pi f$ with respect to the wave vector $\boldsymbol{k}$ [82]

$$\boldsymbol{v} = \frac{\partial(2\pi f)}{\partial \boldsymbol{k}} = \left(\frac{\partial(2\pi f)}{\partial k_x}, \frac{\partial(2\pi f)}{\partial k_y}, \frac{\partial(2\pi f)}{\partial k_z}\right). \tag{A14}$$

Applying Eq. (A14) to Eq. (A13) yields

$$\boldsymbol{v}\Big|_{\boldsymbol{u}\parallel[100]}^{\boldsymbol{k}\parallel[001]} = \frac{\partial(2\pi f)}{\partial \boldsymbol{k}}\Big|_{\boldsymbol{u}\parallel[100]}^{\boldsymbol{k}\parallel[001]} = \left(0, 0, \sqrt{\frac{C_{55}}{\rho}}\right), \tag{A15}$$

thus the magnitude of sound velocity is

$$v\Big|_{\boldsymbol{u}\parallel[100]}^{\boldsymbol{k}\parallel[001]} = \sqrt{\frac{C_{55}}{\rho}}. \tag{A16}$$

Similarly, for the longitudinal mode $\boldsymbol{u} \parallel [001]$ ($u_x = 0$ and $u_y = 0$), we obtain

$$v\Big|_{\boldsymbol{u}\parallel[001]}^{\boldsymbol{k}\parallel[001]} = \sqrt{\frac{C_{33}}{\rho}}. \tag{A17}$$

Note that for these particular cases the sound velocity is parallel to the wave vector ($\boldsymbol{v} \parallel \boldsymbol{k}$), however this relationship do not generally hold in crystals [82]. It is generally true in an isotropic body [82].

Next, for cubic crystals, we may write the effective elastic tensor that includes all MEL effects as

$$C_{ij} = C_{ij}^r + \triangle C_{ij}^J + \triangle C_{ij}^{\mathrm{SOC}}, \tag{A18}$$

where

$$C^r = \begin{pmatrix} C_{11}^r & C_{12}^r & C_{12}^r & 0 & 0 & 0 \\ C_{12}^r & C_{11}^r & C_{12}^r & 0 & 0 & 0 \\ C_{12}^r & C_{12}^r & C_{11}^r & 0 & 0 & 0 \\ 0 & 0 & 0 & C_{44}^r & 0 & 0 \\ 0 & 0 & 0 & 0 & C_{44}^r & 0 \\ 0 & 0 & 0 & 0 & 0 & C_{44}^r \end{pmatrix}, \quad \triangle C^J = \begin{pmatrix} \triangle C_{11}^J & \triangle C_{12}^J & \triangle C_{12}^J & 0 & 0 & 0 \\ \triangle C_{12}^J & \triangle C_{11}^J & \triangle C_{12}^J & 0 & 0 & 0 \\ \triangle C_{12}^J & \triangle C_{12}^J & \triangle C_{11}^J & 0 & 0 & 0 \\ 0 & 0 & 0 & \triangle C_{44}^J & 0 & 0 \\ 0 & 0 & 0 & 0 & \triangle C_{44}^J & 0 \\ 0 & 0 & 0 & 0 & 0 & \triangle C_{44}^J \end{pmatrix},$$

$$\triangle C^{\mathrm{SOC}} = \begin{pmatrix} \triangle C_{11}^{\mathrm{SOC}} & \triangle C_{12}^{\mathrm{SOC}} & \triangle C_{13}^{\mathrm{SOC}} & \triangle C_{14}^{\mathrm{SOC}} & \triangle C_{15}^{\mathrm{SOC}} & \triangle C_{16}^{\mathrm{SOC}} \\ \triangle C_{12}^{\mathrm{SOC}} & \triangle C_{22}^{\mathrm{SOC}} & \triangle C_{23}^{\mathrm{SOC}} & \triangle C_{24}^{\mathrm{SOC}} & \triangle C_{25}^{\mathrm{SOC}} & \triangle C_{26}^{\mathrm{SOC}} \\ \triangle C_{13}^{\mathrm{SOC}} & \triangle C_{23}^{\mathrm{SOC}} & \triangle C_{33}^{\mathrm{SOC}} & \triangle C_{34}^{\mathrm{SOC}} & \triangle C_{35}^{\mathrm{SOC}} & \triangle C_{36}^{\mathrm{SOC}} \\ \triangle C_{14}^{\mathrm{SOC}} & \triangle C_{24}^{\mathrm{SOC}} & \triangle C_{34}^{\mathrm{SOC}} & \triangle C_{44}^{\mathrm{SOC}} & \triangle C_{45}^{\mathrm{SOC}} & \triangle C_{46}^{\mathrm{SOC}} \\ \triangle C_{15}^{\mathrm{SOC}} & \triangle C_{25}^{\mathrm{SOC}} & \triangle C_{35}^{\mathrm{SOC}} & \triangle C_{45}^{\mathrm{SOC}} & \triangle C_{55}^{\mathrm{SOC}} & \triangle C_{56}^{\mathrm{SOC}} \\ \triangle C_{16}^{\mathrm{SOC}} & \triangle C_{26}^{\mathrm{SOC}} & \triangle C_{36}^{\mathrm{SOC}} & \triangle C_{46}^{\mathrm{SOC}} & \triangle C_{56}^{\mathrm{SOC}} & \triangle C_{66}^{\mathrm{SOC}} \end{pmatrix}. \tag{A19}$$

The term C^r corresponds to elastic tensor at the paramagnetic-like state (i.e. with randomly oriented atomic magnetic moments) including only isotropic exchange interaction. The term $\triangle C^J$ gives the correction to the elastic tensor when the isotropic exchange interaction is included and the system is at the ferromagnetic state (parallel collinear spins). Hence, we have

$$\begin{aligned}\triangle C^J_{11} &= C^c_{11} - C^r_{11},\\ \triangle C^J_{12} &= C^c_{12} - C^r_{12},\\ \triangle C^J_{44} &= C^c_{44} - C^r_{44},\end{aligned} \tag{A20}$$

where C^c_{ij} is the elastic tensor when the isotropic exchange interaction is included and the system is at the collinear state. Note that the paramagnetic and collinear states including only the isotropic exchange interaction do not change the cubic crystal symmetry, so that $\triangle C^J$ has the same symmetry as C^r. The term $\triangle C^{\mathrm{SOC}}$ provides the correction to the elastic tensor when SOC is included [18], and depends on the applied magnetic field $\triangle C^{\mathrm{SOC}}(\boldsymbol{H})$. The correction due to SOC can lower the crystal symmetry, so that the symmetries of $\triangle C^{\mathrm{SOC}}$ could be different to C^c and $\triangle C^J$.

In the case of a transverse wave propagating along $\boldsymbol{k} \parallel [001]$ with polarization $\boldsymbol{u} \parallel [100]$, combining Eqs. (A16) and (A18), we find that the fractional change in velocity when the system changes from a paramagnetic state ($C_{55} = C^r_{44}$) to a collinear state including only the isotropic exchange ($C_{55} = C^r_{44} + \triangle C^J_{44} = C^c_{44}$) is

$$\left.\frac{v^c - v^r}{v^r}\right|^{\boldsymbol{k}\parallel[001]}_{\boldsymbol{u}\parallel[100]} = \frac{\sqrt{\frac{C^c_{44}}{\rho^c}} - \sqrt{\frac{C^r_{44}}{\rho^r}}}{\sqrt{\frac{C^r_{44}}{\rho^r}}}. \tag{A21}$$

Similarly, if we include both the isotropic exchange and SOC ($C_{55} = C^r_{44} + \triangle C^J_{44} + \triangle C^{\mathrm{SOC}}_{55} = C^c_{44} + \triangle C^{\mathrm{SOC}}_{55}$), then the fractional change in velocity with respect to the collinear state with only isotropic exchange reads

$$\left.\frac{v^{\mathrm{SOC}} - v^c}{v^c}\right|^{\boldsymbol{k}\parallel[001]}_{\boldsymbol{u}\parallel[100]} = \frac{\sqrt{\frac{C^c_{44}+\triangle C^{\mathrm{SOC}}_{55}}{\rho^{\mathrm{SOC}}}} - \sqrt{\frac{C^c_{44}}{\rho^c}}}{\sqrt{\frac{C^c_{44}}{\rho^c}}}. \tag{A22}$$

In the case of the longitudinal mode, using Eq. (A17), we obtain

$$\left.\frac{v^c - v^r}{v^r}\right|^{\boldsymbol{k}\parallel[001]}_{\boldsymbol{u}\parallel[001]} = \frac{\sqrt{\frac{C^c_{11}}{\rho^c}} - \sqrt{\frac{C^r_{11}}{\rho^r}}}{\sqrt{\frac{C^r_{11}}{\rho^r}}}, \tag{A23}$$

$$\left.\frac{v^{\mathrm{SOC}} - v^c}{v^c}\right|^{\boldsymbol{k}\parallel[001]}_{\boldsymbol{u}\parallel[001]} = \frac{\sqrt{\frac{C^c_{11}+\triangle C^{\mathrm{SOC}}_{33}}{\rho^{\mathrm{SOC}}}} - \sqrt{\frac{C^c_{11}}{\rho^c}}}{\sqrt{\frac{C^c_{11}}{\rho^c}}}. \tag{A24}$$

In this work, we use the elements of the tensor $\triangle C^{\mathrm{SOC}}_{ij}$ calculated by Rinaldi and Turilli [18] for cubic crystals based on the linear MEL theory. Hence, these elements can not describe the high-order effect coming from morphic coefficients [function $G(m)$ in Eq. (20)]. Similarly, they can not account for the rotational-magnetostrictive effect [function $R(\lambda)$ in Eq. (20)] because it requires the finite strain theory [10]. Consequently, the tensor $\triangle C^{\mathrm{SOC}}_{ij}$ calculated by Rinaldi and Turilli [18] can only describe the Simon effect [15], that is, the field dependent term $S(H)$ in Eq. (20) [1]. The elements $\triangle C^{\mathrm{SOC}}_{55}$ and $\triangle C^{\mathrm{SOC}}_{33}$ in Eqs. (A22) and (A24) calculated by Rinaldi and Turilli read [18]

$$\begin{aligned}\triangle C^{\mathrm{SOC}}_{55} &= -\frac{b_2^2}{M_S^2}\left[\left(\alpha^0_z\right)^2\chi_{xx} + \left(\alpha^0_x\right)^2\chi_{zz} + 2\alpha^0_x\alpha^0_z\chi_{xz}\right],\\ \triangle C^{\mathrm{SOC}}_{33} &= -\frac{4b_1^2\left(\alpha^0_z\right)^2\chi_{zz}}{M_S^2},\end{aligned} \tag{A25}$$

where

$$\begin{aligned}\chi_{xx} &= M_S^2\left[\frac{\cos^2\theta_0\cos^2\varphi_0}{E_{\theta\theta}} + \frac{\sin^2\theta_0\sin^2\varphi_0}{E_{\varphi\varphi}}\right],\\ \chi_{xz} &= -M_S^2\frac{\sin\theta_0\cos\theta_0\cos\varphi_0}{E_{\theta\theta}},\\ \chi_{zz} &= M_S^2\frac{\sin^2\theta_0}{E_{\theta\theta}}.\end{aligned} \tag{A26}$$

The quantities $\alpha^0_x = \sin\theta_0\cos\varphi_0$, $\alpha^0_y = \sin\theta_0\sin\varphi_0$, and $\alpha^0_z = \cos\theta_0$ are the equilibrium direction cosine of magnetization that minimizes the magnetic energy E given by

$$\begin{aligned}E(\theta,\varphi) = &\left(K_1 + \frac{b_1^2}{C^c_{11} - C^c_{12}} - \frac{b_2^2}{2C^c_{44}}\right)\\ &\times(\sin^2\theta\cos^2\varphi\sin^2\theta\sin^2\varphi\\ &+ \sin^2\theta\cos^2\varphi\cos^2\theta + \sin^2\theta\sin^2\varphi\cos^2\theta)\\ &- \mu_0 M_s(H_x\sin\theta\cos\varphi + H_y\sin\theta\sin\varphi\\ &+ H_z\cos\theta),\end{aligned} \tag{A27}$$

where

$$\begin{aligned}E_{\theta\theta} &= \frac{1}{2}\frac{\partial^2 E}{\partial\theta^2}\bigg|_{\theta=\theta_0,\varphi=\varphi_0},\\ E_{\varphi\varphi} &= \frac{1}{2}\frac{\partial^2 E}{\partial\varphi^2}\bigg|_{\theta=\theta_0,\varphi=\varphi_0}.\end{aligned} \tag{A28}$$

APPENDIX B: INTERNAL ENERGY IN THE LAGRANGIAN DESCRIPTION

It is convenient to work out the internal energy including high-order terms to facilitate the interpretation of the morphic coefficients calculated with atomistic simulations. In this Appendix, we write the explicit form of the internal energy in the Lagrangian description, as defined by Rouchy *et al.* in Ref. [10]. The internal energy it is expanded in series of the Lagrangian strain tensor η_{ij} which is defined as [10]

$$\eta_{ij} = \varepsilon_{ij} + \frac{1}{2}\sum_k(\varepsilon_{ki} + \omega_{ki})(\varepsilon_{kj} + \omega_{kj}), \tag{B1}$$

where ε_{ij} is given by Eq. (A8) and

$$\omega_{ij} = \frac{1}{2}\left(\frac{\partial u_i}{\partial r_j} - \frac{\partial u_j}{\partial r_i}\right), \qquad i, j = x,\ y,\ \text{and}\ z. \tag{B2}$$

The use of the Lagrangian tensor (finite strain theory) is required to theoretically describe some MEL effects on sound velocity, like the rotational-magnetostrictive effect [function $R(\lambda)$ in Eq. (20)] [1,10,11]. For the analysis of the results given by the atomistic simulations in this work, it may be

enough to consider the following terms in the internal energy per volume [10]

$$E = E_{el}^{I} + E_{el}^{II} + E_{me}^{I} + E_{me}^{II} + E_{a}, \tag{B3}$$

where E_{el}^{I} and E_{el}^{II} are the elastic energy terms up to second and third order in the Lagrangian strain, respectively, E_{me}^{I} and E_{me}^{II} are the MEL energy terms up to first and second order in the Lagrangian strain, respectively, while E_a is the unstrained MCA energy. These terms are given by (cubic crystals, point groups 432, $\bar{4}3m$, $m\bar{3}m$) [10]

$$\begin{aligned}
E_{el}^{I} &= \frac{C_{11}}{2}\left(\eta_{xx}^2+\eta_{yy}^2+\eta_{zz}^2\right) + C_{12}(\eta_{xx}\eta_{yy}+\eta_{xx}\eta_{zz}+\eta_{yy}\eta_{zz}) \\
&\quad + 2C_{44}\left(\eta_{xy}^2+\eta_{yz}^2+\eta_{zx}^2\right), \\
E_{el}^{II} &= \frac{\tilde{C}_{112}}{2}\left(\eta_{xx}^2[\eta_{yy}+\eta_{zz}]+\eta_{yy}^2[\eta_{xx}+\eta_{zz}]+\eta_{zz}^2[\eta_{yy}+\eta_{xx}]\right) \\
&\quad + \tilde{C}_{123}\eta_{xx}\eta_{yy}\eta_{zz} + 2\tilde{C}_{144}\left(\eta_{xx}\eta_{yz}^2+\eta_{yy}\eta_{zx}^2+\eta_{zz}\eta_{xy}^2\right) \\
&\quad + 2\tilde{C}_{155}\left(\eta_{yz}^2[\eta_{yy}+\eta_{zz}]+\eta_{zx}^2[\eta_{zz}+\eta_{xx}]\right. \\
&\quad \left. + \eta_{xy}^2[\eta_{xx}+\eta_{yy}]\right) + 8\tilde{C}_{456}\eta_{xy}\eta_{yz}\eta_{zx}, \\
E_{me}^{I} &= B^{\alpha,2}U^{\alpha}\tilde{K}^{\alpha,2} + B^{\gamma,2}\left[U_1^{\gamma}\tilde{K}_1^{\gamma,2} + U_2^{\gamma}\tilde{K}_2^{\gamma,2}\right] \\
&\quad + B^{\varepsilon,2}\left[U_1^{\varepsilon}\tilde{K}_1^{\varepsilon,2} + U_2^{\varepsilon}\tilde{K}_2^{\varepsilon,2} + U_3^{\varepsilon}\tilde{K}_3^{\varepsilon,2}\right] \\
&= \frac{1}{3}B^{\alpha,2}(\eta_{xx}+\eta_{yy}+\eta_{zz}) + B^{\gamma,2}\left(\left[\alpha_x^2-\frac{1}{3}\right]\eta_{xx}\right. \\
&\quad + \left[\alpha_y^2-\frac{1}{3}\right]\eta_{yy} + \left.\left[\alpha_z^2-\frac{1}{3}\right]\eta_{zz}\right) \\
&\quad + 2B^{\varepsilon,2}(\alpha_y\alpha_z\eta_{yz}+\alpha_z\alpha_x\eta_{zx}+\alpha_x\alpha_y\eta_{xy}), \\
E_{me}^{II} &= \tilde{M}_1^{\alpha,2}\Pi_1^{\alpha}\tilde{K}^{\alpha,2} + \tilde{M}_2^{\alpha,2}\Pi_2^{\alpha}\tilde{K}^{\alpha,2} + \tilde{M}_3^{\alpha,2}\Pi_3^{\alpha}\tilde{K}^{\alpha,2} \\
&\quad + \tilde{M}_1^{\gamma,2}\left[\Pi_{1,1}^{\gamma}\tilde{K}_1^{\gamma,2} + \Pi_{1,2}^{\gamma}\tilde{K}_2^{\gamma,2}\right] + \tilde{M}_2^{\gamma,2}\left[\Pi_{2,1}^{\gamma}\tilde{K}_1^{\gamma,2}\right. \\
&\quad \left. + \Pi_{2,2}^{\gamma}\tilde{K}_2^{\gamma,2}\right] + \tilde{M}_3^{\gamma,2}\left[\Pi_{3,1}^{\gamma}\tilde{K}_1^{\gamma,2} + \Pi_{3,2}^{\gamma}\tilde{K}_2^{\gamma,2}\right] \\
&\quad + \tilde{M}_1^{\varepsilon,2}\left[\Pi_{1,1}^{\varepsilon}\tilde{K}_1^{\varepsilon,2} + \Pi_{1,2}^{\varepsilon}\tilde{K}_2^{\varepsilon,2} + \Pi_{1,3}^{\varepsilon}\tilde{K}_3^{\varepsilon,2}\right] \\
&\quad + \tilde{M}_2^{\varepsilon,2}\left[\Pi_{2,1}^{\varepsilon}\tilde{K}_1^{\varepsilon,2} + \Pi_{2,2}^{\varepsilon}\tilde{K}_2^{\varepsilon,2} + \Pi_{2,3}^{\varepsilon}\tilde{K}_3^{\varepsilon,2}\right] \\
&\quad + \tilde{M}_3^{\varepsilon,2}\left[\Pi_{3,1}^{\varepsilon}\tilde{K}_1^{\varepsilon,2} + \Pi_{3,2}^{\varepsilon}\tilde{K}_2^{\varepsilon,2} + \Pi_{3,3}^{\varepsilon}\tilde{K}_3^{\varepsilon,2}\right], \\
E_a &= \tilde{K}^{\alpha,0}\tilde{K}^{\alpha,2}\tilde{V}^2 + \tilde{K}^{\alpha,0}\tilde{K}^{\alpha,4}\tilde{V}^4,
\end{aligned} \tag{B4}$$

where C_{ij} and $\tilde{C}_{ijk}$ are the second and third order in the Lagrangian strain elastic constants, respectively, B^{μ} and $\tilde{M}_i^{\mu,2}$ ($\mu = \alpha, \beta, \varepsilon$) are the first and second order in the Lagrangian strain MEL constants (up to second order in the direction cosine of magnetization $\boldsymbol{\alpha}$), respectively, while $\tilde{V}^i$ are the MCA constants. The quantities $\tilde{K}_i^{\mu}$ are the cubic harmonic polynomials in terms of $\boldsymbol{\alpha}$, that is [10]

$$\begin{aligned}
&\tilde{K}^{\alpha,0}(\boldsymbol{\alpha}) = \sqrt{3}, \quad \tilde{K}^{\alpha,2}(\boldsymbol{\alpha}) = \frac{1}{\sqrt{3}}, \\
&\tilde{K}^{\alpha,4}(\boldsymbol{\alpha}) = \frac{1}{\sqrt{3}}\left(\alpha_x^4+\alpha_y^4+\alpha_z^4-\frac{3}{5}\right), \\
&\tilde{K}_1^{\gamma,2}(\boldsymbol{\alpha}) = \sqrt{\frac{2}{3}}\left(\alpha_z^2-\frac{\alpha_x^2+\alpha_y^2}{2}\right), \\
&\tilde{K}_2^{\gamma,2}(\boldsymbol{\alpha}) = \frac{1}{\sqrt{2}}\left(\alpha_x^2-\alpha_y^2\right), \quad \tilde{K}_1^{\varepsilon,2}(\boldsymbol{\alpha}) = \sqrt{2}\alpha_y\alpha_z, \\
&\tilde{K}_2^{\varepsilon,2}(\boldsymbol{\alpha}) = \sqrt{2}\alpha_z\alpha_x, \ \tilde{K}_3^{\varepsilon,2}(\boldsymbol{\alpha}) = \sqrt{2}\alpha_x\alpha_y.
\end{aligned} \tag{B5}$$

The quantities U_i^{μ} are linear strain operators for cubic crystals [10]

$$\begin{aligned}
&U^{\alpha} = \frac{1}{\sqrt{3}}(\eta_{xx}+\eta_{yy}+\eta_{zz}), \\
&U_1^{\gamma} = \sqrt{\frac{2}{3}}\left(\eta_{zz}-\frac{\eta_{xx}+\eta_{yy}}{2}\right), \quad U_2^{\gamma} = \frac{1}{\sqrt{2}}(\eta_{xx}-\eta_{yy}) \\
&U_1^{\varepsilon} = \sqrt{2}\eta_{yz}, \quad U_2^{\varepsilon} = \sqrt{2}\eta_{zx}, \quad U_3^{\varepsilon} = \sqrt{2}\eta_{xy},
\end{aligned} \tag{B6}$$

while $\Pi_{i,j}^{\mu}$ are quadratic strain operators for cubic crystals [10]

$$\begin{aligned}
&\Pi_1^{\alpha} = \frac{1}{\sqrt{3}}\left(\eta_{xx}^2+\eta_{yy}^2+\eta_{zz}^2\right), \\
&\Pi_2^{\alpha} = \frac{1}{\sqrt{3}}(\eta_{xx}\eta_{yy}+\eta_{yy}\eta_{zz}+\eta_{xx}\eta_{zz}), \\
&\Pi_3^{\alpha} = \frac{1}{\sqrt{3}}\left(\eta_{yz}^2+\eta_{zx}^2+\eta_{xy}^2\right), \\
&\Pi_{1,1}^{\gamma} = \sqrt{\frac{2}{3}}\left(\eta_{zz}^2-\frac{\eta_{xx}^2+\eta_{yy}^2}{2}\right), \quad \Pi_{1,2}^{\gamma} = \frac{1}{\sqrt{2}}\left(\eta_{xx}^2-\eta_{yy}^2\right) \\
&\Pi_{2,1}^{\gamma} = \sqrt{\frac{2}{3}}\left(\eta_{xx}\eta_{yy}-\frac{\eta_{yy}\eta_{zz}+\eta_{zz}\eta_{xx}}{2}\right), \\
&\Pi_{2,2}^{\gamma} = \frac{1}{\sqrt{2}}(\eta_{yy}\eta_{zz}-\eta_{zz}\eta_{xx}), \\
&\Pi_{3,1}^{\gamma} = \sqrt{\frac{2}{3}}\left(\eta_{xy}^2-\frac{\eta_{yz}^2+\eta_{zx}^2}{2}\right), \quad \Pi_{3,2}^{\gamma} = \frac{1}{\sqrt{2}}\left(\eta_{yz}^2-\eta_{zx}^2\right), \\
&\Pi_{1,1}^{\varepsilon} = \sqrt{2}\eta_{xx}\eta_{yz}, \quad \Pi_{1,2}^{\varepsilon} = \sqrt{2}\eta_{yy}\eta_{zx}, \quad \Pi_{1,3}^{\varepsilon} = \sqrt{2}\eta_{zz}\eta_{xy}, \\
&\Pi_{2,1}^{\varepsilon} = \sqrt{2}(\eta_{yy}+\eta_{zz})\eta_{yz}, \quad \Pi_{2,2}^{\varepsilon} = \sqrt{2}(\eta_{zz}+\eta_{xx})\eta_{zx}, \\
&\Pi_{2,3}^{\varepsilon} = \sqrt{2}(\eta_{xx}+\eta_{yy})\eta_{xy}, \quad \Pi_{3,1}^{\varepsilon} = \sqrt{2}\eta_{zx}\eta_{xy}, \\
&\Pi_{3,2}^{\varepsilon} = \sqrt{2}\eta_{xy}\eta_{yz}, \quad \Pi_{3,3}^{\varepsilon} = \sqrt{2}\eta_{yz}\eta_{zx}.
\end{aligned} \tag{B7}$$

The fractional change in length can be obtained from the minimization of the elastic and MEL energy [83]. It can also be written as an expansion of cubic harmonic polynomials with respect to $\boldsymbol{\alpha}$ and measuring length direction $\boldsymbol{\beta}$, that is [10]

$$\begin{aligned}
\left.\frac{l-l_0}{l_0}\right|_{\boldsymbol{\beta}}^{\boldsymbol{\alpha}} &= \lambda^{\alpha,2}\tilde{K}^{\alpha,2}(\boldsymbol{\alpha})\tilde{K}^{\alpha,2}(\boldsymbol{\beta}) + \lambda^{\gamma,2}\left[\tilde{K}_1^{\gamma,2}(\boldsymbol{\alpha})\tilde{K}_1^{\gamma,2}(\boldsymbol{\beta})\right. \\
&\quad \left. + \tilde{K}_2^{\gamma,2}(\boldsymbol{\alpha})\tilde{K}_2^{\gamma,2}(\boldsymbol{\beta})\right] + \lambda^{\varepsilon,2}\left[\tilde{K}_1^{\varepsilon,2}(\boldsymbol{\alpha})\tilde{K}_1^{\varepsilon,2}(\boldsymbol{\beta})\right. \\
&\quad \left. + \tilde{K}_2^{\varepsilon,2}(\boldsymbol{\alpha})\tilde{K}_2^{\varepsilon,2}(\boldsymbol{\beta}) + \tilde{K}_3^{\varepsilon,2}(\boldsymbol{\alpha})\tilde{K}_3^{\varepsilon,2}(\boldsymbol{\beta})\right] \\
&= \frac{1}{3}\lambda^{\alpha,2} + \lambda^{\gamma,2}\left(\alpha_x^2\beta_x^2+\alpha_y^2\beta_y^2+\alpha_z^2\beta_z^2-\frac{1}{3}\right) \\
&\quad + 2\lambda^{\varepsilon,2}(\alpha_x\alpha_y\beta_x\beta_y+\alpha_y\alpha_z\beta_y\beta_z+\alpha_x\alpha_z\beta_x\beta_z),
\end{aligned} \tag{B8}$$

where

$$\lambda^{\alpha,2} = -\frac{B^{\alpha,2}}{C_{11}+2C_{12}},$$
$$\lambda^{\gamma,2} = -\frac{B^{\gamma,2}}{C_{11}-C_{12}},$$
$$\lambda^{\varepsilon,2} = -\frac{B^{\varepsilon,2}}{C_{44}}. \tag{B9}$$

The morphic coefficients $m_i^{\mu,2}$ are linear combinations of $\tilde{C}_{ijk}$ and $\tilde{M}_i^{\mu,2}$ and are given by [10]

$$\begin{aligned}
m_1^{\alpha,2} &= \tilde{M}_1^{\alpha,2} + \frac{1}{2}(\tilde{C}_{111}+2\tilde{C}_{112})\lambda^{\alpha,2},\\
m_3^{\alpha,2} &= \tilde{M}_2^{\alpha,2} + (\tilde{C}_{123}+2\tilde{C}_{112})\lambda^{\alpha,2},\\
m_3^{\alpha,2} &= \tilde{M}_3^{\alpha,2} + 2(\tilde{C}_{144}+2\tilde{C}_{155})\lambda^{\alpha,2},\\
m_1^{\gamma,2} &= \tilde{M}_1^{\gamma,2} + \frac{1}{2}(\tilde{C}_{111}-\tilde{C}_{112})\lambda^{\gamma,2},\\
m_3^{\gamma,2} &= \tilde{M}_2^{\gamma,2} + (\tilde{C}_{123}-\tilde{C}_{112})\lambda^{\gamma,2},\\
m_3^{\gamma,2} &= \tilde{M}_3^{\gamma,2} + 2(\tilde{C}_{144}-\tilde{C}_{155})\lambda^{\gamma,2},\\
m_1^{\varepsilon,2} &= \tilde{M}_1^{\varepsilon,2} + 2\tilde{C}_{144}\lambda^{\varepsilon,2},\\
m_3^{\varepsilon,2} &= \tilde{M}_2^{\varepsilon,2} + 2\tilde{C}_{155}\lambda^{\varepsilon,2},\\
m_3^{\varepsilon,2} &= \tilde{M}_3^{\varepsilon,2} + 4\tilde{C}_{456}\lambda^{\varepsilon,2}.
\end{aligned} \tag{B10}$$

The definitions for $m_i^{\mu,2}$ and $\tilde{M}_i^{\mu,2}$ are the same as in Ref. [10], but note that they are different to the expressions used in Ref. [1]. The MEL constants $B^{\mu,2}$, magnetostrictive coefficients $\lambda^{\mu,2}$ and MCA constant $\tilde{V}^4$ are related to the corresponding properties of the spin-lattice model given in Table II through [54]

$$\lambda^{\gamma,2} = \frac{3}{2}\lambda_{001}, \quad \lambda^{\varepsilon,2} = \frac{3}{2}\lambda_{111},$$
$$B^{\gamma,2} = b_1, \quad B^{\varepsilon,2} = b_2, \quad \tilde{V}^4 = -\frac{K_1}{2}. \tag{B11}$$

One final remark about the definition of the MEL constants. By restricting the following analysis to the infinitesimal strain theory, where the Lagrangian tensor η_{ij} is replaced by the strain tensor ε_{ij}, the MEL energy E_{me}^I in Eq. (B4) becomes

$$\begin{aligned}
E_{me}^I = {} & \frac{1}{3}B^{\alpha,2}(\varepsilon_{xx}+\varepsilon_{yy}+\varepsilon_{zz})\\
& + B^{\gamma,2}\left(\left[\alpha_x^2-\frac{1}{3}\right]\varepsilon_{xx} + \left[\alpha_y^2-\frac{1}{3}\right]\varepsilon_{yy} + \left[\alpha_z^2-\frac{1}{3}\right]\varepsilon_{zz}\right)\\
& + 2B^{\varepsilon,2}(\alpha_y\alpha_z\varepsilon_{yz}+\alpha_z\alpha_x\varepsilon_{zx}+\alpha_x\alpha_y\varepsilon_{xy}).
\end{aligned} \tag{B12}$$

This term is typically rewritten using other definition of the MEL constants as [83]

$$\begin{aligned}
E_{me}^I = {} & b_0(\varepsilon_{xx}+\varepsilon_{yy}+\varepsilon_{zz}) + b_1\left(\alpha_x^2\varepsilon_{xx}+\alpha_y^2\varepsilon_{yy}+\alpha_z^2\varepsilon_{zz}\right)\\
& + 2b_2(\alpha_x\alpha_y\varepsilon_{xy}+\alpha_x\alpha_z\varepsilon_{xz}+\alpha_y\alpha_z\varepsilon_{yz}),
\end{aligned} \tag{B13}$$

where

$$b_0 = \frac{1}{3}(B^{\alpha,2}-B^{\gamma,2}), \quad B^{\alpha,2} = 3b_0+b_1. \tag{B14}$$

From a mathematical point of view, both forms of the MEL energy are equivalent. However, the definition of MEL constants in Eq. (B12) has the advantage that fully decouples the isotropic and anisotropic magnetic interactions, which might be helpful in a systematic theoretical analysis of the effects of magnetic interactions on MEL phenomena. Namely, $B^{\alpha,2}$ contains all contribution to the MEL energy from isotropic magnetic interactions like the isotropic exchange, while $B^{\gamma,2}$ and $B^{\varepsilon,2}$ contain all contribution to the MEL energy provided by anisotropic magnetic interactions like SOC and crystal field interactions [1]. This means that b_0 has contributions from both the isotropic and anisotropic magnetic interactions, as shown by Eq. (B14). For example, we can also see this fact in the relationship between volume magnetostriction (induced by the isotropic exchange) and MEL constants

$$\omega_s \simeq \lambda^{\alpha,2} = -\frac{B^{\alpha,2}}{C_{11}+2C_{12}} = -\frac{3b_0+b_1}{C_{11}+2C_{12}}, \tag{B15}$$

where b_0 cannot account for the entire contribution of isotropic exchange interaction to ω_s by itself.

APPENDIX C: NUMERICAL TESTS

During the production of this work we identified possible issues in the implementation of the applied magnetic field ($\boldsymbol{H}$) and anisotropy field ($\boldsymbol{H}_K$) in the SPIN package [52] of LAMMPS [46]. In this Appendix, we provide two numerical tests that helped us to verify the correct implementation of these quantities. We recommend to perform similar tests before running complex spin-lattice simulations involving $\boldsymbol{H}$ and $\boldsymbol{H}_K$ in the spin dynamics.

1. Test for the applied magnetic field

As a general rule to verify the correct implementation of any quantity in a simulation, it is convenient to design a simple test that only involves this particular quantity in order to avoid additional effects on the results coming from other possible issues. Similarly, exact analytical solutions could be helpful in these tests to identify possible missing factors in the program implementation easily. For example, we can check the applied magnetic field $\boldsymbol{H}$ through the analysis of the precession of the atomic magnetic moments. To simplify the theoretical analysis, we only perform spin dynamics (frozen lattice) at zero temperature without damping in the Landau-Lifshitz-Gilbert (LLG) equation ($\lambda_{\mathrm{LLG}} = 0$). Moreover, in the spin model we set an initial collinear state and only include the Zeeman term in the Heisenberg Hamiltonian [first term in the right-hand side of Eq. (2)]. Hence, under these conditions, the equation of motion of each normalized magnetic moment $\boldsymbol{s}_i = \boldsymbol{\mu}_i/\mu_i$ is reduced to

$$\frac{d\boldsymbol{s}_i}{dt} = -\gamma(\boldsymbol{s}_i \times \mu_0\boldsymbol{H}), \tag{C1}$$

where $\gamma = 1.76\times10^{11}\ \mathrm{T^{-1}\,s^{-1}}$ is the gyromagnetic ratio and μ_0 is the vacuum permeability. Assuming the applied magnetic field along the z axis, the exact analytical solution of this differential equation for the x component of each normalized magnetic moment $s_{x,i}$ is

$$s_{x,i}(t) = s_{x,i}(0)\cos(2\pi f_{\mathrm{prec}}t), \tag{C2}$$

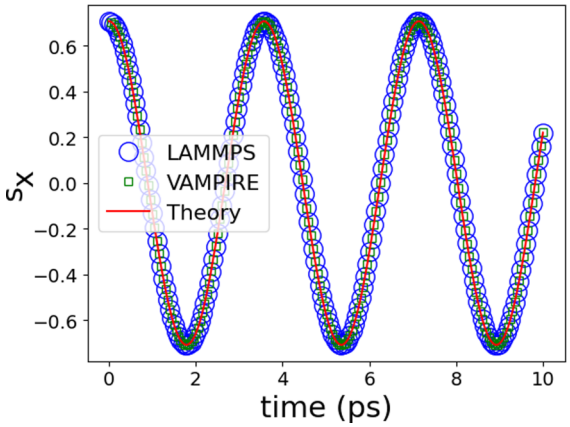

FIG. 12. Test for the correct implementation of the applied magnetic field. Simulated dynamics of the x-component of the normalized magnetic moment s_x with (blue circles) the SPIN package [52] of LAMMPS [46] and (green squares) VAMPIRE code [44]. The red line represents the theoretical solution given by Eq. (C2). The initial direction of the normalized magnetic moment is $s_x(0) = 1/\sqrt{2}$, $s_y(0) = 0$, and $s_z(0) = 1/\sqrt{2}$, while the applied magnetic field is $\mu_0 H = 10$ T along the z axis.

where the precession frequency is

$$f_{\text{prec}} = \frac{\gamma \mu_0 H}{2\pi}. \tag{C3}$$

Therefore, to check the correct implementation of $\boldsymbol{H}$ in the program, one can compare the theoretical solution [Eq. (C2)] with the numerical result given by the simulation. This test is shown in Fig. 12 using an initial direction of the normalized magnetic moments $s_x(0) = 1/\sqrt{2}$, $s_y(0) = 0$, and $s_z(0) = 1/\sqrt{2}$, and applied magnetic field $\mu_0 H = 10$ T along the z axis. Here, we also double checked the result with the atomistic spin dynamics program VAMPIRE [44].

2. Test for the anisotropy field

The following numerical test to verify the correct implementation of the anisotropy field ($\boldsymbol{H}_K$) is inspired by the Sucksmith-Thompson method [84] that is typically used to measure the MCA constant of uniaxial magnets with easy axis ($K_u > 0$) in experiment. Let us consider a single domain magnet with easy axis MCA, so that the magnetic energy per volume is given by the Stoner Wohlfarth model [84]

$$\frac{E}{V} = K_u \sin^2\theta - \mu_0 M_S H \cos(\Theta - \theta), \tag{C4}$$

where $K_u > 0$ (easy axis), θ and Θ are the angles between the magnetization $\boldsymbol{M}$ and applied field $\boldsymbol{H}$ with respect to the z axis (easy axis), respectively. Now, we set the applied field along the x axis ($\boldsymbol{H} = (H, 0, 0)$, $\Theta = \pi/2$) and find the equilibrium x component of magnetization ($M_{x,\text{eq}}$) by minimizing the total energy with respect to $M_x = M_S \sin\theta$, that is

$$\frac{\partial}{\partial M_x}\frac{E}{V} = 0 \rightarrow \frac{M_{x,\text{eq}}}{M_S} = \frac{H}{H_K}, \tag{C5}$$

where

$$H_K = \frac{2K_u}{\mu_0 M_S}. \tag{C6}$$

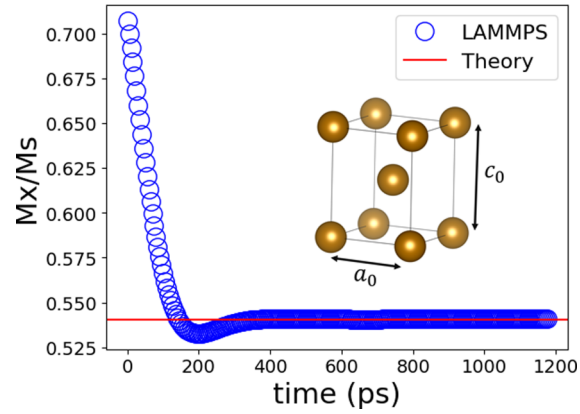

FIG. 13. Test for the correct implementation of the anisotropy field. Simulated dynamics of the x component of the normalized magnetization M_x/M_S with (blue circles) the SPIN package [52] of LAMMPS [46] for BCC Fe under a tetragonal deformation $\tau = c_0/a_0 = 1.02$, where $a_0 = 2.83023$ Å. The red line represents the theoretical equilibrium x-component of the normalized magnetization $M_{x,\text{eq}}/M_S$ given by Eq. (C9). The initial direction of the normalized magnetization is $M_x(0)/M_s = 1/\sqrt{2}$, $M_y(0)/M_s = 0$, and $M_z(0)/M_s = 1/\sqrt{2}$, while the applied magnetic field is $\mu_0 \boldsymbol{H} = (0.05, 0, 0)$ T. In this test, we used the parameters given in Sec. II B, but we don't include the quadrupole term [$q(r_{ij}) = 0$] in order to be consistent with the theoretical derivation of Eq. (C9). Moreover, we perform only spin dynamics (frozen lattice) with high LLG damping to speed up the convergence to the equilibrium state.

Therefore, to check the anisotropy field in the program, we can compare the theoretical x component of magnetization at equilibrium [Eq. (C5)] with the numerical result obtained in the simulation. To this end, we consider the spin-lattice model described in Sec. II (two-ion anisotropy) for BCC Fe under a tetragonal deformation in order to induce an effective uniaxial anisotropy (K_u). To simplify the following theoretical analysis of the Néel model, we consider a collinear state at zero temperature, only spin dynamics (frozen lattice) and we don't include the quadrupole term of the Néel model ($q(r_{ij}) = 0$). Using Eq. (5), we find that the effective uniaxial MCA constant (K_u) can be written in terms of the dipole term [$l(r_{ij})$] of the Néel model as

$$\begin{aligned} K_u &= \frac{n_{\text{at}}}{V}[\mathcal{H}_{\text{Néel}}(\boldsymbol{s} = (1,0,0)) - \mathcal{H}_{\text{Néel}}(\boldsymbol{s} = (0,0,1))] \\ &= -\frac{4l(r_0)n_{\text{at}}}{V}\frac{1-\tau^2}{2+\tau^2}, \end{aligned} \tag{C7}$$

where n_{at} is the number of atoms in the volume V, $\tau = c_0/a_0$ is the ratio between the lattice parameters c_0 and $a_0 = b_0$ (tetragonal deformation) and $r_0 = (a_0/2)\sqrt{2+\tau^2}$. Note the selected parameters in Eq. (C7) for this test should lead to an easy axis ($K_u > 0$). Replacing Eq. (C7) in Eq. (C6) yields the following anisotropy field

$$H_K = -\frac{8l(r_0)}{\mu_0 \mu}\frac{1-\tau^2}{2+\tau^2}, \tag{C8}$$

where μ is the atomic magnetic moment. Here, we also used the expression $M_s = n_{\text{at}}\mu/V$. Hence, replacing Eq. (C8) in

Eq. (C5) gives

$$\frac{M_{x,\mathrm{eq}}}{M_S} = \frac{H}{H_K} = -\frac{\mu\mu_0 H}{8l(r_0)}\frac{2+\tau^2}{1-\tau^2}. \tag{C9}$$

This test is shown in Fig. 13 using an initial direction of the normalized magnetization $M_x(0)/M_s = 1/\sqrt{2}$, $M_y(0)/M_s = 0$, and $M_z(0)/M_s = 1/\sqrt{2}$, and applied magnetic field $\mu_0 \boldsymbol{H} = (0.05, 0, 0)$ T. The applied tetragonal deformation is $\tau = c_0/a_0 = 1.02$, where $a_0 = 2.83023$ Å. In this simulation we used the parameters given in Sec. II B, but we don't include the quadrupole term ($q(r_{ij}) = 0$) in order to be consistent with the theoretical derivation of Eq. (C9). Moreover, we perform only spin dynamics (frozen lattice) with high LLG damping to speed up the convergence to the equilibrium state. Note that this test involves also the applied magnetic field, so that it is convenient to verify it first through the test described previously in Sec. C 1. A similar test as this one could also be used to verify the correct implementation of the anisotropy field in a spin model with other types of MCA like the one-ion anisotropy [38,55].

[1] E. D. T. de Lacheisserie, *Magnetostriction: Theory and Application of Magnetoelasticity* (CRC Press, Boca Raton, FL, 1993).
[2] J. P. Joule, Ann. Electr. Magn. Chem **8**, 219 (1842).
[3] D. Malyugin, J. Magn. Magn. Mater. **97**, 193 (1991).
[4] C. Matteucci, Ann. Chim. Phys. **53** (1858).
[5] E. Wasserman, *Handbook of Ferromagnetic Materials* (Elsevier, North Holland, Amsterdam, 1990), Vol. 5, pp. 237–322.
[6] L. Benito, M. Ciria, A. Fraile, D. Fort, J. S. Abell, and J. I. Arnaudas, Phys. Rev. Lett. **98**, 267201 (2007).
[7] D. T. Adroja, A. del Moral, C. de la Fuente, A. Fraile, E. A. Goremychkin, J. W. Taylor, A. D. Hillier, and F. Fernandez-Alonso, Phys. Rev. Lett. **108**, 216402 (2012).
[8] K. Fuchs and A. M. Tyndall, Proc. R. Soc. London A **153**, 622 (1936).
[9] H. Mueller, Phys. Rev. **58**, 805 (1940).
[10] J. Rouchy and E. du Tremolet de Lacheisserie, Z. Phys. B **36**, 67 (1979).
[11] J. Rouchy, E. T. de Lacheisserie, J. Genna, and A. Waintal, J. Magn. Magn. Mater. **21**, 69 (1980).
[12] I. Isenberg, Phys. Rev. **83**, 637 (1951).
[13] W. P. Mason, Phys. Rev. **82**, 715 (1951).
[14] D. E. Eastman, Phys. Rev. **148**, 530 (1966).
[15] G. Simon, Z. Naturforsch. A **13**, 84 (1958).
[16] H. Sato, J. Appl. Phys. **29**, 456 (1958).
[17] J. Sakurai, J. Phys. Soc. Jpn. **19**, 311 (1964).
[18] S. Rinaldi and G. Turilli, Phys. Rev. B **31**, 3051 (1985).
[19] E. du Tremolet de Lacheisserie and J. Rouchy, J. Magn. Magn. Mater. **28**, 77 (1982).
[20] J. Rouchy, P. Morin, and E. T. de Lacheisserie, J. Magn. Magn. Mater. **23**, 59 (1981).
[21] G. Alers, J. Neighbours, and H. Sato, J. Phys. Chem. Solids **9**, 21 (1959).
[22] G. Dietz and G. Wielpütz, Appl. Phys. **11**, 131 (1976).
[23] C. Kingner, J. Heil, and B. Lüthi, J. Appl. Phys. **52**, 2270 (1981).
[24] M. Seavey, Solid State Commun. **10**, 219 (1972).
[25] K. Uchida, H. Adachi, T. An, T. Ota, M. Toda, B. Hillebrands, S. Maekawa, and E. Saitoh, Nat. Mater. **10**, 737 (2011).
[26] I. S. Camara, J.-Y. Duquesne, A. Lemaître, C. Gourdon, and L. Thevenard, Phys. Rev. Applied **11**, 014045 (2019).
[27] O. Kovalenko, T. Pezeril, and V. V. Temnov, Phys. Rev. Lett. **110**, 266602 (2013).
[28] L. Thevenard, J.-Y. Duquesne, E. Peronne, H. J. von Bardeleben, H. Jaffres, S. Ruttala, J.-M. George, A. Lemaître, and C. Gourdon, Phys. Rev. B **87**, 144402 (2013).
[29] L. Thevenard, I. S. Camara, S. Majrab, M. Bernard, P. Rovillain, A. Lemaître, C. Gourdon, and J.-Y. Duquesne, Phys. Rev. B **93**, 134430 (2016).
[30] V. S. Vlasov, A. M. Lomonosov, A. V. Golov, L. N. Kotov, V. Besse, A. Alekhin, D. A. Kuzmin, I. V. Bychkov, and V. V. Temnov, Phys. Rev. B **101**, 024425 (2020).
[31] A. Stupakiewicz, C. S. Davies, K. Szerenos, D. Afanasiev, K. S. Rabinovich, A. V. Boris, A. Caviglia, A. V. Kimel, and A. Kirilyuk, Nat. Phys. **17**, 489 (2021).
[32] W. Li, B. Buford, A. Jander, and P. Dhagat, IEEE Trans. Magn. **50**, 37 (2014).
[33] S. Westmoreland, R. Evans, G. Hrkac, T. Schrefl, G. Zimanyi, M. Winklhofer, N. Sakuma, M. Yano, A. Kato, T. Shoji *et al.*, Scr. Mater. **148**, 56 (2018).
[34] D. Hinzke, U. Atxitia, K. Carva, P. Nieves, O. Chubykalo-Fesenko, P. M. Oppeneer, and U. Nowak, Phys. Rev. B **92**, 054412 (2015).
[35] N. Kazantseva, D. Hinzke, U. Nowak, R. W. Chantrell, U. Atxitia, and O. Chubykalo-Fesenko, Phys. Rev. B **77**, 184428 (2008).
[36] O. Hubert, J. Magn. Magn. Mater. **491**, 165564 (2019).
[37] X. Wu, Z. Liu, and T. Luo, J. Appl. Phys. **123**, 085109 (2018).
[38] R. F. L. Evans, U. Atxitia, and R. W. Chantrell, Phys. Rev. B **91**, 144425 (2015).
[39] A. Neogi and N. Mitra, Sci. Rep. **7**, 7337 (2017).
[40] T. Wejrzanowski, M. Spychalski, R. Pielaszek, and K. J. Kurzydlowski, in *Multiscale Kinetic Modelling of Materials*, Solid State Phenomena Vol. 129 (Trans Tech, Switzerland, Uetikon, 2007), pp. 145–150.
[41] P. Nieves, S. Arapan, T. Schrefl, and S. Cuesta-Lopez, Phys. Rev. B **96**, 224411 (2017).
[42] H. Huang and H. Van Swygenhoven, MRS Bull. **34**, 160 (2009).
[43] V. Besse, A. Golov, V. Vlasov, A. Alekhin, D. Kuzmin, I. Bychkov, L. Kotov, and V. Temnov, J. Magn. Magn. Mater. **502**, 166320 (2020).
[44] R. F. L. Evans, W. J. Fan, P. Chureemart, T. A. Ostler, M. O. A. Ellis, and R. W. Chantrell, J. Phys.: Condens. Matter **26**, 103202 (2014).
[45] O. Eriksson, A. Bergman, L. Bergqvist, and J. Hellsvik, *Atomistic Spin Dynamics* (Oxford University Press, Oxford, 2017).
[46] A. P. Thompson, H. M. Aktulga, R. Berger, D. S. Bolintineanu, W. M. Brown, P. S. Crozier, P. J. in't Veld, A. Kohlmeyer, S. G. Moore, T. D. Nguyen *et al.*, Comput. Phys. Commun. **271**, 108171 (2022).

[47] I. Stockem, A. Bergman, A. Glensk, T. Hickel, F. Körmann, B. Grabowski, J. Neugebauer, and B. Alling, Phys. Rev. Lett. **121**, 125902 (2018).
[48] P.-W. Ma, C. H. Woo, and S. L. Dudarev, Phys. Rev. B **78**, 024434 (2008).
[49] D. Beaujouan, P. Thibaudeau, and C. Barreteau, Phys. Rev. B **86**, 174409 (2012).
[50] P.-W. Ma, S. Dudarev, and C. Woo, Comput. Phys. Commun. **207**, 350 (2016).
[51] D. Perera, D. M. Nicholson, M. Eisenbach, G. M. Stocks, and D. P. Landau, Phys. Rev. B **95**, 014431 (2017).
[52] J. Tranchida, S. Plimpton, P. Thibaudeau, and A. Thompson, J. Comput. Phys. **372**, 406 (2018).
[53] S. Nikolov, M. A. Wood, A. Cangi, J.-B. Maillet, M.-C. Marinica, A. P. Thompson, M. P. Desjarlais, and J. Tranchida, npj Comput. Mater. **7**, 153 (2021).
[54] P. Nieves, J. Tranchida, S. Arapan, and D. Legut, Phys. Rev. B **103**, 094437 (2021).
[55] R. Skomski, *Simple Models of Magnetism* (Oxford University Press, Oxford, 2008).
[56] S. Chikazumi, *Physics of Ferromagnetism* (Oxford University Press, Oxford, 2009).
[57] K.-H. Yang and J. O. Hirschfelder, Phys. Rev. A **22**, 1814 (1980).
[58] A. P. Thompson, L. P. Swiler, C. R. Trott, S. M. Foiles, and G. J. Tucker, J. Comput. Phys. **285**, 316 (2015).
[59] R. C. O'Handley *Modern Magnetic Materials Principles and Applications* (Wiley, New York, 2000).
[60] M. Shimizu, J. Phys. Soc. Jpn. **44**, 792 (1978).
[61] F. D. Murnaghan, Proc. Natl. Acad. Sci. U.S.A. **30**, 244 (1944).
[62] C. L. Fu and K. M. Ho, Phys. Rev. B **28**, 5480 (1983).
[63] S. Zhang and R. Zhang, Comput. Phys. Commun. **220**, 403 (2017).
[64] P. Nieves, S. Arapan, S. Zhang, A. Kadzielawa, R. Zhang, and D. Legut, Comput. Phys. Commun. **264**, 107964 (2021).
[65] J. A. Rayne and B. S. Chandrasekhar, Phys. Rev. **122**, 1714 (1961).
[66] B.-J. Lee, J.-H. Shim, and M. I. Baskes, Phys. Rev. B **68**, 144112 (2003).
[67] M. Getzlaff, *Fundamentals of Magnetism* (Springer, Berlin, Heidelberg, 2008).
[68] T. Burkert, O. Eriksson, P. James, S. I. Simak, B. Johansson, and L. Nordström, Phys. Rev. B **69**, 104426 (2004).
[69] A. Kia, A. Mitra, C. Weinberger, and W. Cai, Wave propagation in solids using molecular dynamics, Term Project Report, Stanford University, 2004.
[70] A. Togo and I. Tanaka, Scr. Mater. **108**, 1 (2015).
[71] Phonopy, https://phonopy.github.io/phonopy.
[72] A. Carreras, Phonolammps, https://github.com/abelcarreras/phonolammps.
[73] R. Truell, C. Elbaum, and B. B. Chick, in *Ultrasonic Methods in Solid State Physics*, edited by R. Truell, C. Elbaum, and B. B. Chick (Academic Press, 1969), pp. 53–158, https://www.sciencedirect.com/science/article/pii/B9781483233185500079.
[74] R. N. Thurston and K. Brugger, Phys. Rev. **133**, A1604 (1964).
[75] T. Ikeda, Jpn. J. Appl. Phys. **21**, 1249 (1982).
[76] B. Alling, T. Marten, and I. A. Abrikosov, Phys. Rev. B **82**, 184430 (2010).
[77] W. B. Nurdin and K.-D. Schotte, Phys. Rev. E **61**, 3579 (2000).
[78] D. Doane, J. Magn. Magn. Mater. **5**, 184 (1977).
[79] Y. Ikeda, A. Seko, A. Togo, and I. Tanaka, Phys. Rev. B **90**, 134106 (2014).
[80] I. Novikov, B. Grabowski, F. Körmann, and A. Shapeev, npj Comput. Mater. **8**, 13 (2022).
[81] P.-W. Ma and S. L. Dudarev, Phys. Rev. B **86**, 054416 (2012).
[82] L. D. Landau and E. M. Lifshitz, *Theory of Elasticity / by L. D. Landau and E. M. Lifshitz; translated from the Russian by J. B. Sykes and W. H. Reid* (Pergamon, London, 1959).
[83] A. Clark, *Handbook of Ferromagnetic Materials* (Elsevier, North Holland, Amsterdam, 1980), Vol. 1, pp. 531–589.
[84] R. Skomski and J. M. D. Coey, *Permanent Magnetism* (Institute of Physics, Bristol, 1999).